



Quantum simulations in effective model spaces: Hamiltonian-learning variational quantum eigensolver using digital quantum computers and application to the Lipkin-Meshkov-Glick model

Caroline E. P. Robin ^{1,2,*} and Martin J. Savage ^{3,†}

¹*Fakultät für Physik, Universität Bielefeld, D-33615 Bielefeld, Germany*

²*GSI Helmholtzzentrum für Schwerionenforschung, Planckstraße 1, D-64291 Darmstadt, Germany*

³*InQubator for Quantum Simulation (IQUS), Department of Physics, University of Washington, Seattle, Washington 98195, USA*



(Received 4 March 2023; accepted 25 July 2023; published 18 August 2023)

Background: Quantum simulations offer the potential to predict the structure and dynamics of nuclear many-body systems that are beyond the capabilities of classical computing. Generally, preparing the ground state of strongly interacting many-body systems relevant to nuclear physics is, however, inefficient, even using ideal quantum computers. In addition, currently available noisy intermediate-scale quantum (NISQ) era quantum devices possess modest numbers of qubits, limiting the size of quantum many-body systems that can be simulated. In this context, a reformulation of the quantum many-body problems using truncated model spaces and Hamiltonians is desirable to make them more amenable to near-term quantum computers. The importance of symmetries in low-energy theories, including effective field theories (EFTs), lattice quantum chromodynamics (QCD), and effective model spaces for nuclear systems, in particular their interplay with the reduction of active Hilbert spaces, is well known. Lesser known is the fact that the noncommutivity of some symmetries and truncations of the model space can be profitably combined with variational calculations to rearrange the entanglement into localized structures and enable more efficient simulations.

Purpose: The goal of the present study is to explore and utilize the noncommutivity of symmetries and model-space truncations of quantum many-body systems important to nuclear physics, particularly in combination with variational algorithms for quantum simulations and effective Hamiltonian learning.

Method: We introduce an iterative hybrid classical-quantum algorithm, the Hamiltonian learning variational quantum eigensolver (HL-VQE), that simultaneously optimizes an effective Hamiltonian, thereby rearranging entanglement into the effective model space, and the associated ground-state wave function. Quantum simulations, using classical computers and IBM's superconducting-qubit quantum computers, are performed to demonstrate the HL-VQE algorithm, in the context of the Lipkin-Meshkov-Glick (LMG) model of interacting fermions, where the Hamiltonian transformation corresponds to an orbital rotation. We use a mapping where the number of qubits scales with the logarithm of the size of the effective model space, rather than the particle number.

Results: HL-VQE is found to provide an exponential improvement in LMG-model calculations of the ground-state energy and wave function, compared to naive truncations without Hamiltonian learning, throughout a significant fraction of the Hilbert space. In the context of EFT, this corresponds to counterterms scaling exponentially with the cutoff as opposed to power law. Implementations on IBM's QExperience quantum computers and simulators for one- and two-qubit effective model spaces are shown to provide accurate and precise results, reproducing classical predictions.

Conclusions: For a range of parameters defining the LMG model, the HL-VQE algorithm is found to have better scaling of quantum resources requirements than previously explored algorithms. In particular, the HL-VQE scales efficiently over a large fraction of the model space, in contrast to VQE alone. This work constitutes a step in the development of entanglement-driven quantum algorithms for descriptions of nuclear many-body systems. This, in part, leverages the potential of noisy intermediate-scale quantum (NISQ) devices. The exponential scaling of counterterms observed in this study suggests the possibility of more general applicability to other nonperturbative EFTs.

DOI: [10.1103/PhysRevC.108.024313](https://doi.org/10.1103/PhysRevC.108.024313)

I. INTRODUCTION

Future quantum computers will allow us to predict the properties and dynamics of physically relevant quantum many-body systems that are inaccessible to classical computing [1–10], including nuclei and dense matter. It is the capability to control and maintain coherence, entanglement, and

*crobin@physik.uni-bielefeld.de

†On leave from the Institute for Nuclear Theory; mjs5@uw.edu

quantum correlations that allows some classically inefficient simulations to be performed efficiently with (ideal) quantum computers. One of the major features of such devices is the linear scaling of the memory requirement (number of qubits) needed to map a full N -particle Hilbert space. However, even with this capability, the required time for solving some important nuclear many-body problems on quantum computers in an exact way generally remains superpolynomial in the number of particles, residing in the QMA complexity class [11], rather than in BQP. This scaling can be mitigated by applying truncations of the full Hilbert space and Hamiltonian to render the problem solvable in polynomial time. Such truncations, which can be made in space-time, of the continuous fields, in the dimensionality of local Hilbert spaces, and so forth, are usually justified because only a subset of the Hilbert space is expected to be relevant to the description of ground or low-lying excited states. Furthermore, currently available quantum devices, in addition, suffer from important limitations such as noise, limited number of qubits and connectivity, as well as gate and measurement errors. In this context, truncations of the Hilbert space allow for a reduction of the circuit sizes, in terms of both qubit and gate numbers, decreasing the noise and errors, thus making such circuits more suitable for implementation on current noisy intermediate-scale quantum (NISQ) [12] devices. Extracting meaningful predictions from the truncated spaces then requires a complete quantification of uncertainties in the simulations, and therefore theoretical and algorithmic understandings of these truncations is essential (for a recent review, see, for example, Ref. [13]).

In addition to truncations of the model space, simulations of systems with truncated “nearby” Hamiltonians, with systematically removable deviations from a target Hamiltonian, can also provide reliable results [13], if the associated uncertainty is within the target uncertainty of the computation. In this context, the use of effective field theory (EFT) naturally lends itself, as, in principle, the order of truncation of the EFT can be matched to the size of the simulation error through an iterative tuning procedure [13]. EFTs, effective interactions, and effective model spaces have been extensively employed in modern nuclear physics for the simulations of few- and many-baryon systems, and have provided new pathways for classical simulations to address quantities of interest, well before reliable predictions from quantum chromodynamics (QCD) become possible [14–17]. It is also the means by which lattice QCD calculations furnish results for low-lying processes. The simulated Hamiltonian(s) derived from, for example, EFT and variants thereof can be systematically improved in support of more precise numerical computations of the systems of interest as they become practical. In the context of quantum simulations, an expansion of the EFT to higher orders can be made as experimental progress is achieved in building quantum devices.

For an EFT to be predictive, it must capture the low-energy degrees of freedom with effective interactions that systematically recover S -matrix elements order by order in an expansion (that may or may not involve non-perturbative resummations), with a power-counting defined in the context of a regularization and renormalization scheme. The challenge in applying EFTs to nuclear systems is the size of

the expansion parameters, which can be uncomfortably large, and establishing a consistent power-counting scheme. Classic examples of EFTs that are useful for nuclear physics are chiral perturbation theory (χ PT) [18,19], heavy-baryon chiral perturbation theory (HB χ PT) [20], and nuclear EFT [21–24], which are designed to implement the approximate global chiral symmetries of QCD. These techniques continue to be merged with more traditional nuclear shell-model and effective model-space frameworks (see, e.g., Ref. [25] for a recent review), so that predictions for nuclei and multi-nucleon systems are consistent with QCD. Ultimately, the objective of the EFT program is to match effective nuclear forces to QCD, which can then be used in nuclear many-body calculations performed in effective model spaces, for the description of both structure properties and dynamical processes, e.g., as discussed in Refs. [14,26]. In the area of quantum simulations of dynamics, it has recently been shown that product formula can be used to evolve states in a low-energy space forward in time with only exponentially small leakage into the high-energy space [27], consistent with the rigorous use of effective model spaces and EFTs.

The present work has emerged from considerations of entanglement as an organizing principle for nuclear structure calculations [28–42]. In a previous study [33], we analyzed the entanglement structures of single-particle orbitals emerging from *ab initio* no-core configuration-interaction calculations of light nuclei. In particular, we investigated how transformations of the single-particle basis into a natural basis could minimize and rearrange entanglement into a localized part of the Hilbert space. Including two-nucleon correlations in light nuclei to define variational natural (VNAT) single-particle orbitals localized the one-orbital entanglement entropy around the Fermi level, and eliminated two-orbital negativity in the nuclear wave function. The variational character of the VNAT basis was found to restrict the two-orbital mutual information to the truncated space and decoupled the inactive space. In that sense, the VNAT basis minimizes the number of many-body basis states necessary to describe the nuclear wave function, and reduces the loss of information originating from the model-space truncation. More recently, the valence-space density matrix renormalization group (VS-DMRG) has been used to compute orbital entanglement entropy and mutual information in *sd*-shell nuclei, to motivate a reorganization of orbitals [40].

Following our earlier work, we investigate whether the localization of entanglement structures can be utilized in designing efficient quantum simulations of nuclear many-body systems amenable to quantum computers, including NISQ devices. Our present study takes a step in that direction, and demonstrates that an orbital transformation, equivalent to transformation of the Hamiltonian, provides an efficient mechanism for including quantum correlations in low-lying states of a model many-body system in quantum simulations, and is also potentially useful for classical simulations.

The widely appreciated Lipkin-Meshkov-Glick (LMG) model is a useful “sandbox” for testing new ideas that may have applicability (to varying degrees) to realistic nuclear systems and forces. The separation of scales in realistic systems means that the ideas developed within the LMG model have

also been helpful in those systems. Its rich phenomenology from a simple Hamiltonian provides sufficient complexity that has led to a number of previous studies that explore quantum correlations and entanglement [36–38,43–48], quantum algorithms [49–52], and more, to develop understanding and techniques that can be applied to quantum simulations of nuclei and multinucleon systems. Previous quantum simulations of the LMG model [49–52] have directly mapped the elementary SU(2) spaces associated with each fermion to qubits in the quantum computer (or classical simulator). In this way VQE has been used to determine the ground state of few-nucleon systems in the model [49] using IBM’s quantum computers [53], and ADAPT-VQE [54,55] has been used to examine systems of up to $N = 12$ nucleons using a classical simulator [51]. That extensive study explored the behavior of ADAPT-VQE building upon the trivial $0p-0h$ state and also the Hartee-Fock ground state. The authors also applied their techniques to valence model spaces of nuclei in the sd and pf shells, with interesting results, concluding that there could be substantial benefits to applying such quantum algorithms to nuclear structure calculations. One of these studies [52] also considered a number of other mappings, including the J -space mapping (that we utilize in this work) and binary encoding of the occupation number with consideration of the efficient Gray code, with good results obtained for the ground states, and also excited states, for small systems.

In this work, we examine the utility of effective model spaces for hybrid classical-quantum simulations of nuclear many-body systems. Specifically, we explore potential advantages of simultaneously learning the effective-model-space Hamiltonian and finding the ground-state wave function in the LMG model, introducing the Hamiltonian-Learning-VQE algorithm, which is similar to the orbital-optimized VQE (oo-VQE) algorithm used by quantum chemists [56,57], but differing in the truncation used in defining the effective model space(s). The truncation we employ more closely resembles that employed in the EFTs mentioned above, aligning to a greater extent with the Wilsonian renormalization group organization, than with the coupled-clusters truncation(s) used in quantum chemistry. The optimized ground state in the one-dimensional effective model space corresponds to the Hartee-Fock state, while the ground state in larger spaces systematically and self-consistently includes higher-body correlations. The exponential improvement in convergence of the estimated ground-state energy that we find from the optimization, means that the VQE algorithm, which naively scales poorly on quantum devices, scales favorably when the Hamiltonian in the effective model space is also learned.

The main points emerging from the present work are

- (i) The use of EFTs and effective model spaces for quantum simulations of nuclear structure calculations is explored in the context of the Lipkin-Meshkov-Glick model. Simultaneously optimizing the effective Hamiltonian and ground-state wave function in (truncated) effective model spaces, using the ground-state energy as the cost-function, leads to exponential improvements in the ground-state energies and wave functions throughout a significant fraction of the

Hilbert space over naive truncations of the Hamiltonian. We anticipate that the ideas and results are broadly applicable.

- (ii) A Hamiltonian learning variation of the VQE algorithm, HL-VQE, is introduced that simultaneously optimizes the Hamiltonian and variational ground-state wave function in a truncated model space, that is amenable to quantum simulations and scales efficiently [because of the above observation(s)]. The algorithm is hybrid-classical-quantum, where expectation values of the Hamiltonian and its gradients are evaluated using a quantum computer, while the variations of the Hamiltonian and wave function parameters are performed classically.
- (iii) Quantum simulations in effective model spaces using one and two qubits are performed using IBM’s quantum computer `ibm_lagos`, which is one of the IBM Quantum Falcon Processors [53], and simulator AER using the QISKIT [58] API. These simulations demonstrate techniques and workflows that could be implemented on more capable quantum computers, providing results that recover the exponential convergence of ground-state energies and wave function fidelities.

The outline of the paper is as follows: Section II introduces the LMG model in detail, particularly its representation in terms of SU(2) angular momentum states and the corresponding Hamiltonian in that basis. These results naturally lend themselves to considering effective model spaces and effective Hamiltonians with a variational parameter associated with global rotations. This is detailed in Sec. III, which presents results obtained with classical calculations for the convergence of the ground-state energy and wave function fidelity for selected model parameters and system sizes, along with an overview of the theoretical fabric defining the logic of the effective model space calculations. The algorithms, techniques, quantum circuits, gradient descent, and more associated with the HL-VQE algorithm that we use for quantum simulations performed using IBM’s quantum computers are detailed in Sec. IV. Results obtained from one- and two-qubit quantum simulations using `ibm_lagos` and classical simulator AER are presented and discussed in Sec. V, where estimates of quantum resources required for simulations using more capable quantum computers are also provided. In Sec. VI, we conclude and summarize the results of this work.

II. THE LIPKIN-MESHKOV-GLICK MODEL

The Lipkin-Meshkov-Glick (LMG) model [59] describes a system of N interacting fermions, each distributed between two levels separated by an energy ϵ , labeled by $\sigma = \pm$. Each level is N -fold degenerate, with (noninteracting) single-particle states labeled by $p = 1, 2, \dots, N$.¹ This is

¹This is equivalent to a system of $N s = \frac{1}{2}$ particles immersed in a magnetic field, where each spin interacts with all of the others [43,44].

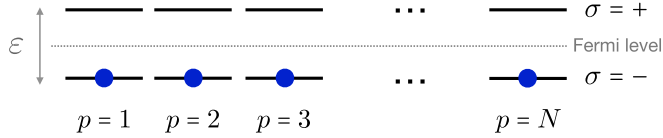


FIG. 1. Lowest-energy noninteracting (0p-0h) configuration of a system of N particles in the LMG model.

illustrated in Fig. 1, which shows the lowest-energy, or zero-particle-zero-hole (0p-0h), noninteracting configuration of the system. In the LMG model, the particles are assumed to interact via a monopole-monopole interaction that scatters pairs of particles between states of the upper and lower levels having the same value of p . The Hamiltonian governing the system has the form

$$\begin{aligned} \hat{H} &= \frac{\varepsilon}{2} \sum_{\sigma p} \sigma c_{p\sigma}^\dagger c_{p\sigma} - \frac{V}{2} \sum_{pq\sigma} c_{p\sigma}^\dagger c_{q\sigma}^\dagger c_{q-\sigma} c_{p-\sigma} \\ &= \varepsilon \hat{J}_z - \frac{V}{2} (\hat{J}_+^2 + \hat{J}_-^2), \end{aligned} \quad (1)$$

where the operators $c_{p\sigma}^\dagger$ and $c_{p\sigma}$ create and destroy a fermion in level σ of state p , respectively, and \hat{J}_z , \hat{J}_+ , \hat{J}_- are collective quasi-spin operators defined as

$$\begin{aligned} \hat{J}_z &= \frac{1}{2} \sum_{p\sigma} \sigma c_{p\sigma}^\dagger c_{p\sigma}, \\ \hat{J}_+ &= \sum_p c_{p+}^\dagger c_{p-}, \\ \hat{J}_- &= (J_+)^{\dagger} = \sum_p c_{p-}^\dagger c_{p+}, \end{aligned} \quad (2)$$

which generate an $\text{su}(2)$ algebra.

The Hamiltonian in Eq. (1) preserves a number of symmetries. In particular, it conserves rotational invariance so that (exact) eigenstates $|\Psi_{\text{ex}}^{(J)}\rangle$ of \hat{H} can be expanded in the basis $\{|J, M\rangle\}$ formed by eigenstates of \hat{J}^2 and \hat{J}_z as

$$|\Psi_{\text{ex}}^{(J)}\rangle = \sum_{M=-J}^J A_{J,M} |J, M\rangle. \quad (3)$$

Exact solutions can then be obtained via diagonalization of the Hamiltonian in the $\{|J, M\rangle\}$ basis, which is equivalent to minimizing the energy of the system with respect to the coefficients $\{A_{J,M}\}$. In the present work, we are interested in determining the ground state, which corresponds to diagonalization in the block characterized by $J = N/2$. The quantum number M , eigenvalue of \hat{J}_z , denotes the different noninteracting configurations of the system. For instance, the configuration where all particles are in the lower level (0p-0h configuration) corresponds to $|J = N/2, M = -N/2\rangle$ (see Fig. 1), the configurations with one particle in the upper level (1p-1h configurations) are contained in $|J = N/2, M = 1 - N/2\rangle$, and so on, up to the configuration where all N particles are in the upper level ($Np-Nh$), which corresponds to $|J = N/2, M = N/2\rangle$. In the rest of the paper, we will thus adopt the following short-hand notation to denote the

many-body basis states:

$$|n\rangle \equiv \left| J = \frac{N}{2}, M = n - J = n - \frac{N}{2} \right\rangle, \quad (4)$$

where n denotes the excitation order ($np-nh$) of the state.

The specific form of the interaction in Eq. (1) also preserves the number of particles in a given state p (because V scatters particles between states with same value of p), which is associated with the operator

$$\hat{N}_p = \sum_{\sigma} c_{p\sigma}^\dagger c_{p\sigma}, \quad (5)$$

with $\langle \Psi_{\text{ex}}^{(J)} | \hat{N}_p | \Psi_{\text{ex}}^{(J)} \rangle = 1$, as well as ‘‘parity’’ symmetry (sometimes referred to as number-parity symmetry [51]) associated with

$$\hat{\Pi} = e^{i\pi \hat{N}_+}, \quad (6)$$

where

$$\hat{N}_+ = \sum_p c_{p+}^\dagger c_{p+} = \hat{J}_z + \frac{N}{2} \quad (7)$$

counts the number of particles in the $\sigma = +$ upper level. The configurations with an even (odd, respectively) number of particles in the upper level are eigenstates of $\hat{\Pi}$ with eigenvalue $+1$ (-1 , respectively):

$$\hat{\Pi} |n\rangle = (-1)^n |n\rangle. \quad (8)$$

This parity symmetry is due to the fact that V only scatters pairs of particles.

The matrix elements of the Hamiltonian in Eq. (1) are

$$\langle n' | \hat{H} | n \rangle = \varepsilon C_n^z \delta_{n',n} - \frac{V}{2} (C_n^+ \delta_{n',n+2} + C_n^- \delta_{n',n-2}), \quad (9)$$

where

$$\begin{aligned} C_n^z &= M = n - J, \\ C_n^+ &= \sqrt{J(J+1) - M(M+1)} \sqrt{J(J+1) - (M+1)(M+2)}, \\ &= \sqrt{J(J+1) - (n-J)(n-J+1)} \\ &\quad \times \sqrt{J(J+1) - (n-J+1)(n-J+2)}, \\ C_n^- &= \sqrt{J(J+1) - M(M-1)} \sqrt{J(J+1) - (M-1)(M-2)}, \\ &= \sqrt{J(J+1) - (n-J)(n-J-1)} \\ &\quad \times \sqrt{J(J+1) - (n-J-1)(n-J-2)}. \end{aligned} \quad (10)$$

Thus the Hamiltonian only connects configurations with excitation orders differing by zero or two units, as imposed by the parity symmetry. Consequently, the interacting ground state will be restricted to a superposition of even- n components (0p-0h, 2p-2h, \dots), while states with odd- n configurations (1p-1h, 3p-3h, \dots) will correspond to excited states.

It is worth briefly considering the behavior of the system in the $N \rightarrow \infty$ limit. With appropriate rescaling, the discrete states map toward a continuum in n -space, and the Hamiltonian matrix can be identified with the finite-difference form of a second-order differential equation. For a range of Hamiltonian parameters, the lowest-lying solutions of the equation have wave functions that fall exponentially for

large-, and consequently, the energy difference between the lowest-lying even- and odd-parity states falls exponentially with N , while the gap to the first excited states (with same parity as the ground state) tends to a nearly N -independent value. Thus, the ground state of the LMG-Hamiltonian is doubly degenerate in the large- N limit, with states of opposite parity that are gapped to nearest excitations.²

III. EFFECTIVE MODEL SPACES FOR THE LIPKIN-MESHKOV-GLICK MODEL

When all configurations are included in Eq. (3), the solution does not depend on the single-particle basis that is used to build the configurations $|n\rangle$. In realistic many-body calculations, however, one is typically forced to truncate such an expansion in order to make the diagonalization problem tractable. Once a truncation is made, the solution will depend on the nature of the single-particle states, which can also be optimized via a variational principle. Minimizing the energy with respect to both expansion coefficients and orbitals corresponds to the approach known as the multiconfiguration self-consistent field (MCSCF) method in quantum chemistry (see, e.g., Ref. [62]). This approach has also been applied to classical calculations of nuclear systems [63,64], and showed good entanglement properties in *ab initio* calculations of light nuclei [33]. In particular, it was found that the optimized orbitals led to an increased localization of quantum correlations within the basis.

In the LMG model, in order to preserve the rotational invariance and the symmetry associated with the operator \hat{N}_p in Eq. (5), the orbital transformation between the original and optimized single-particle bases is restricted to only mix states of the lower and upper levels with the same value of p . This can be written as a unitary transformation corresponding to a rotation of the individual quasispins around the y axis by an angle β , as

$$\begin{pmatrix} c_{p+}(\beta) \\ c_{p-}(\beta) \end{pmatrix} = \begin{pmatrix} \cos(\beta/2) & -\sin(\beta/2) \\ \sin(\beta/2) & \cos(\beta/2) \end{pmatrix} \begin{pmatrix} c_{p+} \\ c_{p-} \end{pmatrix}. \quad (11)$$

where $c_{p\sigma} \equiv c_{p\sigma}(\beta = 0)$ is the operator annihilating a particle in the original single-particle state (p, σ) . After this rotation, a truncation can be made by imposing a cutoff Λ in the summation in Eq. (3) to include np - nh configurations with $n \leq \Lambda - 1$. The effective (truncated) many-body state becomes

$$|\Psi\rangle^{(\Lambda)} = \sum_{n=0}^{\Lambda-1} A_n^{(\beta)} |n, \beta\rangle, \quad (12)$$

where the basis states $|n, \beta\rangle$ are np - nh configurations built on the rotated single-particle basis. In Eq. (12), $|\Psi\rangle^{(\Lambda)} \equiv |\Psi\rangle^{(\Lambda)}(\beta)$ with the explicit β dependence omitted in what follows.

The effective Hamiltonian can then be written in terms of the rotated collective quasispin operators,

$\hat{J}(\beta) = \hat{U}^\dagger(\beta) \hat{J} \hat{U}(\beta)$, where $\hat{U}(\beta) = e^{-i\hat{J}_y \beta}$, as

$$\begin{aligned} \hat{H}(\beta) &\equiv U^\dagger(\beta) \hat{H} U(\beta) \\ &= \varepsilon \left[\cos \beta \hat{J}_z(\beta) + \frac{1}{2} \sin \beta [\hat{J}_+(\beta) + \hat{J}_-(\beta)] \right] \\ &\quad - \frac{V}{4} [\sin^2 \beta [4\hat{J}_z(\beta)^2 - \{\hat{J}_+(\beta), \hat{J}_-(\beta)\}] \\ &\quad + (1 + \cos^2 \beta) [\hat{J}_+(\beta)^2 + \hat{J}_-(\beta)^2] - 2 \sin \beta \cos \beta \\ &\quad \times [\{\hat{J}_z(\beta), \hat{J}_+(\beta)\} + \{\hat{J}_z(\beta), \hat{J}_-(\beta)\}]], \end{aligned} \quad (13)$$

where the $\hat{J}_{z,\pm}(\beta)$ operators can be expressed in terms of $c_{p\sigma}(\beta)$ and $c_{p\sigma}^\dagger(\beta)$ in analogy with Eq. (2) (see Appendix A for details), and $\{\hat{A}, \hat{B}\} = \hat{A}\hat{B} + \hat{B}\hat{A}$ denotes an anticommutator. This unitary transformation of the Hamiltonian preserves the energy eigenvalues in the absence of truncation, but modifies the eigenvalues for arbitrary Λ . $\hat{H}(\beta)$ thus represents an effective Hamiltonian acting in the truncated many-body space. We see from Eq. (13) that this effective Hamiltonian connects states $|n, \beta\rangle$ and $|n \pm 1, \beta\rangle$ (when $\beta \neq 0$), thus the summation in Eq. (12) now runs over both even and odd values of n . The corresponding matrix elements of $\hat{H}(\beta)$ are given in Appendix A. The angle β and set of coefficients $\{A_n^{(\beta)}\}$ are determined by applying a variational principle to the energy of the system $E(\Lambda) = \langle \Psi^{(\Lambda)} | \hat{H}(\beta) | \Psi^{(\Lambda)} \rangle - \eta \langle \Psi^{(\Lambda)} | \Psi^{(\Lambda)} \rangle$, where η is a Lagrange parameter ensuring normalization of the many-body state $|\Psi\rangle^{(\Lambda)}$.

The transformed and truncated effective Hamiltonian in Eq. (13) is not expected to be complete in the sense of exactly reproducing energy eigenvalues for the Λ levels, but is expected to capture the one-body mean-field contributions and systematically include the effect of correlations beyond mean-field with increasing Λ . To put this construction in the framework of low-energy EFT, beyond the leading-order (LO) Hamiltonian in Eq. (13) there are additional operators with coefficients (counterterms) that are required to be determined by matching to the full theory. In the analysis that follows, these coefficients are set equal to zero, and we focus on optimizing results from the LO Hamiltonian. Interestingly, comparisons with the exact results show that the omitted contributions from the counterterms are exponentially suppressed with increasing Λ for $\Lambda \ll N$, above which an unexpected plateau region is found; see Sec. III B. In the context of mapping to the register of a quantum computer, this exponential behavior corresponds to double-exponential behavior with respect to the number of qubits.

To recover the approximation to the exact state in Eq. (3) from the effective state $|\Psi\rangle^{(\Lambda)}$ in Eq. (12), it is useful to reexpress $|\Psi\rangle^{(\Lambda)}$ in the original unrotated basis ($\beta = 0$) as

$$|\Psi\rangle^{(\Lambda)} = \sum_{m=0}^N A_m^{(\beta=0)} |m, \beta = 0\rangle, \quad (14)$$

where

$$A_m^{(\beta=0)} = \sum_{n=0}^{\Lambda-1} A_n^{(\beta)} \langle m, \beta = 0 | n, \beta \rangle. \quad (15)$$

²The ground-state sector of the LMG model with particular Hamiltonian parameters possesses properties for a variant of a parity-encoded logical qubit [60,61].

Note that the summation in Eq. (14) is not limited to a certain cutoff, and thus includes all possible configurations (up to Np - Nh configurations). The overlap between many-body basis states built on the original and rotated single-particle states are simply given by the matrix representing the rotation of angle β around axis y as

$$\begin{aligned} \langle m, \beta = 0 | n, \beta \rangle &= \langle J, M' = m - J | e^{iJ_y \beta} | J, M = n - J \rangle \\ &\equiv d_{M'=m-J, M=n-J}^J(\beta), \end{aligned} \quad (16)$$

with $J = N/2$ and (see, e.g., Ref. [65])

$$\begin{aligned} d_{M', M}^J(\beta) &= \left(\frac{(J+M')!(J-M')!}{(J+M)!(J-M)!} \right)^{1/2} \sum_s \binom{J+M}{J-M'-s} \\ &\times \binom{J-M}{s} (-1)^{J-M'-s} (\cos \beta/2)^{2s+M'+M} \\ &\times (\sin \beta/2)^{2J-2s-M'-M}, \end{aligned} \quad (17)$$

where the sum over s is restricted by $1/(n!) = 0$ for $n < 0$.

Given the nature of the wave function obtained in an effective model space, $|\Psi\rangle^{(\Lambda)}$, a projection onto states of good parity, $|\Psi\rangle_{\pm}^{(\Lambda)}$, should be subsequently performed, which can be obtained from

$$|\Psi\rangle_{\pm}^{(\Lambda)} = \frac{1}{2}(\mathbb{1} \pm \Pi)|\Psi\rangle^{(\Lambda)}. \quad (18)$$

It is straightforward to see from the matrix elements of $H(\beta)$ (see Appendix A) that the states $|\Psi\rangle^{(\Lambda)}$ and $\hat{\Pi}|\Psi\rangle^{(\Lambda)} = \sum_{n \leq \Lambda-1} A_n^{(\beta)} (-1)^n |n, -\beta\rangle$ are degenerate. In the unrotated basis, the projection procedure amounts to canceling the coefficients $A_m^{(\beta=0)}$ for odd values of m for the case of $|\Psi\rangle_{+}^{(\Lambda)}$, and even values of m for $|\Psi\rangle_{-}^{(\Lambda)}$, followed by a rescaling of the coefficients to normalize $|\Psi\rangle_{\pm}^{(\Lambda)}$ to 1. Note that, in this work, we perform the projection after the minimization procedure. In nuclear physics this is usually referred to as ‘‘projection after variation’’ [66]. Techniques for projecting quantum states in quantum simulations of nuclear many-body systems have been developed in Refs. [67–70].

To quantify the rate of convergence of the approximate wave function with respect to the size of the model space, we will compute the Bures distance [71] $D_B(\Lambda)$ as a measure of the distance between the exact state $|\Psi_{\text{ex}}\rangle$ given in Eq. (3) and the effective projected state $|\Psi\rangle_{+}^{(\Lambda)}$ given in Eq. (18):

$$D_B(\Lambda) = \sqrt{2(1 - |\langle \Psi_{\text{ex}} | \Psi \rangle_{+}^{(\Lambda)}|)}, \quad (19)$$

which we find to be a more useful measure of fidelity for our purposes, as opposed to the usual overlap of states. Figure 2 summarizes the successive steps of the calculation. The minimization of the ground-state energy in an effective model space can be performed using classical computers (this section), or using quantum or hybrid classical-quantum computations (see Secs. IV and V). As mentioned above, in the case of the LMG model, the Hamiltonian \hat{H} preserves the parity symmetry associated with the operator $\hat{\Pi}$ in Eq. (6). This symmetry is broken by the transformation $\hat{U}(\beta)$ and thus needs to be restored. We perform this restoration subsequently

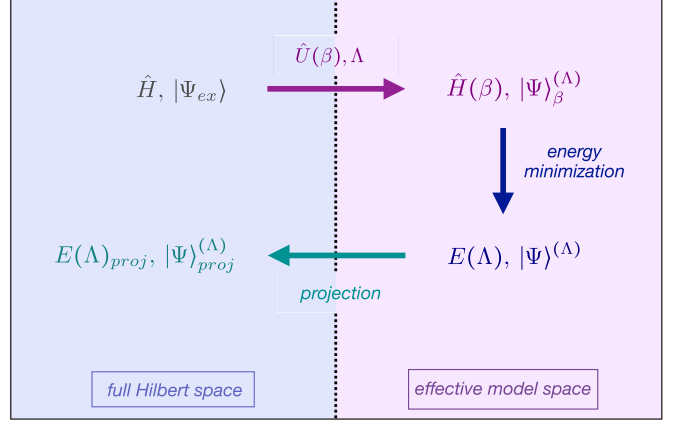


FIG. 2. Flow chart of the calculation. Starting from the full-space Hamiltonian \hat{H} given in Eq. (1), with exact eigenvectors $|\Psi_{\text{ex}}\rangle$, an effective model space is defined, characterized by a given cutoff Λ , as well as a unitary transformation $\hat{U}(\beta)$ corresponding to a rotation of the quasipin operators by angle β . The transformed Hamiltonian $\hat{H}(\beta) = \hat{U}^\dagger(\beta)\hat{H}\hat{U}(\beta)$, defined in Eq. (13), possesses the same eigenvalues as \hat{H} . However, the goal is to determine the optimal transformation $\hat{U}(\beta)$ so that the truncated transformed Hamiltonian, diagonalized in the effective model space Λ , reproduces the ground-state energy of the full Hamiltonian with only a small error. Such an optimal value of the angle β is determined via a variational principle applied to the energy of the system.

to the calculation according to Eq. (18). Note that the projection introduces components outside of the truncated model space Λ . We emphasize, however, that the need for projection is specific to the LMG model studied here. The forces governing realistic nuclear systems do not possess the symmetry associated with the operator $\hat{\Pi}$, and the effective state in the MCSCF approach typically preserves the symmetries of the Hamiltonian [63].

A. Example system: $N = 30$

In order to gain physical insight into the model, and to illustrate the capability of the method, we first investigate both the energy and wave function of the ground state, obtained from classical calculations, using different values of the cutoff Λ for a system of $N = 30$ particles.

The truncation $\Lambda = 1$ corresponds to the Hartree-Fock (HF) limit, i.e., when the many-body state is restricted to the configuration $|n = 0, \beta\rangle$, where all particles occupy the lower level of the rotated basis. This approximation has been extensively studied (see, e.g., Ref. [72]), and it is well known that in this case β becomes nonzero above a critical value of the ratio of the single-particle and interaction terms in the Hamiltonian $\bar{v} = (N - 1)V/\varepsilon$. In particular, the transition to a parity-broken (‘‘deformed’’) phase occurs at $\bar{v} = 1.0$. Figure 3 shows the relative difference between the exact and HF energy (green curve), as a function of \bar{v} . As is well known, the HF approximation works best for large values of \bar{v} , away from the phase transition, where the error drops below 1%. Close to the phase transition, correlations beyond HF are required for a correct description of the system. This is illustrated by the

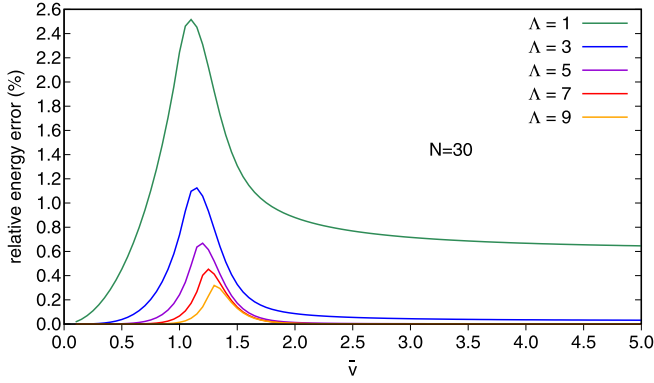


FIG. 3. Relative error $|\frac{E_{\text{ex}} - E(\Lambda)}{E_{\text{ex}}}|$ (in %) in the ground state energy as a function of \bar{v} , obtained for different values of the cutoff Λ , for a system of $N = 30$ particles.

other curves of Fig. 3, which have been obtained with cutoff values $\Lambda = 3, 5, 7, 9$.

In the following, we examine the behavior of the ground-state wave function away from and around the phase transition, obtained with two different values of the interaction ratio $\bar{v} = 2.0$ and $\bar{v} = 1.2$, respectively. Figure 4 shows the composition of the many-body wave function in terms of the components $|n, \beta\rangle$ built on the rotated basis, for the case $\bar{v} = 2.0$. The corresponding values of β obtained variationally for each cutoff Λ are shown in Table I. Note that when Λ takes an even value, the configuration with maximal excitation order $n = \Lambda - 1$ is always found to have zero amplitude in the wave function (see Appendix C for discussion). This is why the results in Table I do not change when $\Lambda \rightarrow \Lambda + 1$ for odd Λ . We see that as Λ (and thus the model space) increases, the angle β decreases, and the wave function becomes fragmented into several components. For low values of Λ , the wave function remains well localized around the $n = 0$ configuration in the effective model space, and the contribution from higher n states decreases rapidly. This rapid falloff is expected to increase the efficiency of the quantum simulations (performed in Sec. V). As $\Lambda \rightarrow N$ we observe a transition towards a parity-unbroken phase ($\beta = 0$) at $\Lambda = 21$, and we find that the

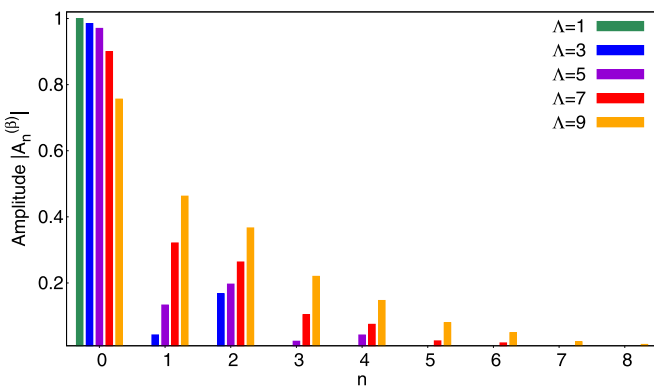


FIG. 4. Absolute value of the amplitudes $A_n^{(\beta)}$ in the effective wave function, obtained for $N = 30$, $\bar{v} = 2.0$, and different cutoff values.

TABLE I. Values of the angle β obtained for different values of the cutoff Λ , for a system of $N = 30$ particles, and $\bar{v} = 2.0$. The solution obtained for even values of Λ is the same as for the odd cutoff $\Lambda' = \Lambda - 1$ (see discussion in Appendix C).

Λ	β	Λ	β
1,2	1.047	17,18	0.289
3,4	1.016	19,20	0.150
5,6	0.977	21,22	0.0
7,8	0.906	23,24	0.0
9,10	0.791	25,26	0.0
11,12	0.664	27,28	0.0
13,14	0.538	29,30	0.0
15,16	0.415	31	0.0

wave function evolves towards the exact (full-Hilbert-space) solution.

The transformation in Eq. (17) is implemented in order to compare the exact and effective (truncated) wave functions. The results are shown in Fig. 5 for the case $\Lambda = 3$. The black histograms show the exact wave function, which is distributed over ≈ 10 states, from 0p-0h to 20p-20h, and is peaked around 6p-6h and 8p-8h. The light blue histograms correspond to the effective wave function expressed in the original $\beta = 0$ basis, as in Eq. (14). The trend of the exact distribution is rather well reproduced, however, we observe nonzero contributions from states characterized by odd values of m . These odd- m components are due to the fact that the transformation Eq. (11) breaks the parity symmetry associated with the operator $\hat{\Pi}$ in Eq. (6) since

$$\hat{\Pi}|n, \beta\rangle = (-1)^n|n, -\beta\rangle, \quad (20)$$

and thus the state $|\Psi\rangle^{(\Lambda)}$ in Eq. (12) is no longer eigenstate of $\hat{\Pi}$. One should therefore project $|\Psi\rangle^{(\Lambda)}$ onto a parity-preserving state $|\Psi\rangle_{\pm}^{(\Lambda)}$, as discussed in the previous section around Eq. (18). The dark blue histograms in Fig. 5 correspond to the effective wave function expressed in the original $\beta = 0$ basis, after projection onto a good parity state

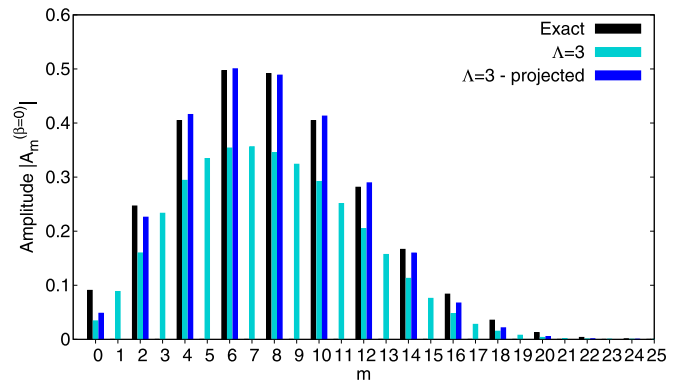


FIG. 5. Absolute value of the amplitudes $A_m^{(\beta=0)}$ in the effective wave function [see Eq. (14)], obtained for $N = 30$, $\bar{v} = 2.0$, and $\Lambda = 3$. The light are dark blue histograms show the results before and after projection onto a good-parity state, respectively. For comparison the exact wave function is shown in black.

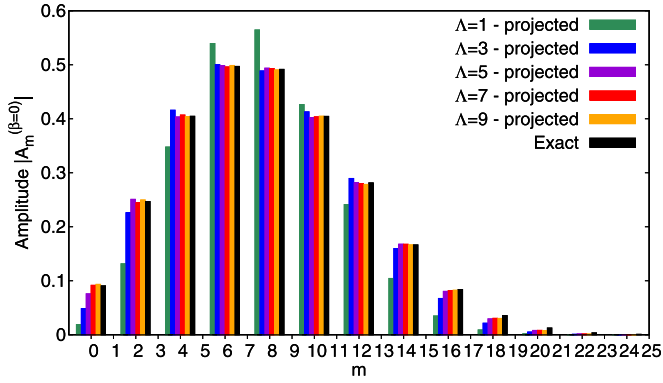


FIG. 6. Absolute value of the amplitudes $A_m^{(\beta=0)}$ obtained after projection of the effective wave function, for $N = 30$, $\bar{v} = 2.0$, and different cutoff values.

via Eq. (18). Even though there remain discrepancies in the tails of the distribution, the $\Lambda = 3$ states in the effective space well recover the exact wave function. These discrepancies are rapidly corrected as Λ increases. This can be seen from Fig. 6 which displays the convergence of the effective wave function in the original $\beta = 0$ basis. The Bures distance is displayed in Fig. 7 as a function of the cutoff Λ (red points). For comparison we also show the Bures distance between the exact state and the truncated state with fixed value of $\beta = 0$ (black points). Evidently, applying a truncation to the model space without rotating the single-particle basis only yields a polynomial convergence of the wave function. In contrast, when β is determined variationally, the convergence is accelerated and matches an exponential behavior, up to $\Lambda = 15$. For $\Lambda > 15$ the Bures distance increases from its local minimum value in order to recover the $\beta = 0$ (symmetry-unbroken) solution at $\Lambda = 21$, as shown in Table I.

It is also interesting to study the behavior of the system around the phase transition. For example we consider here the case $\bar{v} = 1.2$. Figures 8 and 9 show the amplitude of the configurations built on the rotated and original ($\beta = 0$) bases, respectively. The corresponding optimal values of the angle

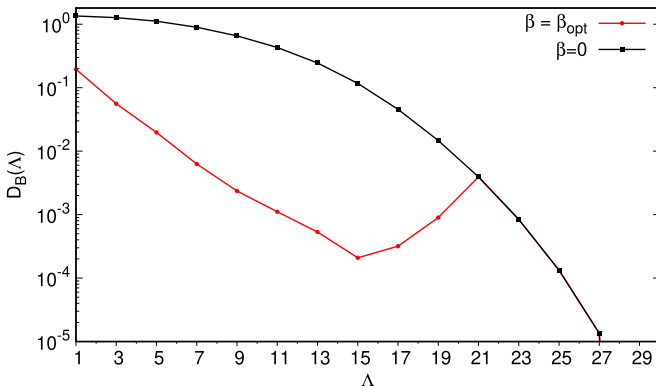


FIG. 7. Bures distance $D_B(\Lambda)$ [Eq. (19)] as a function of the cutoff Λ for $N = 30$ and $\bar{v} = 2.0$. The red points show the results obtained when optimizing the angle β via the variational principle, while the black points are the results obtained with $\beta = 0$.

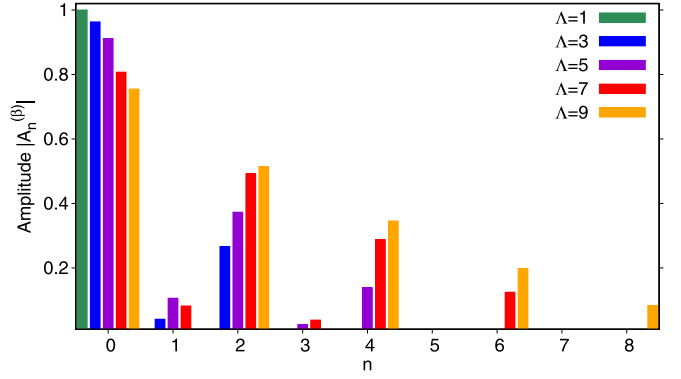


FIG. 8. Absolute value of the amplitudes $A_n^{(\beta)}$ in the effective wave function, obtained for $N = 30$, $\bar{v} = 1.2$, and different cutoff values.

β are shown in Table II. Figure 9 shows that the HF ($\Lambda = 1$) approximation leads to a poor description of the wave function in the region near the phase transition. This was already pointed out in the original paper [72]. In particular, the weight of the $m = 0$ basis state (0p-0h) is largely underestimated, while the contributions of the $m = 2$ and $m = 4$ states (2p-2h and 4p4h) are significantly overestimated, compared to the exact solution. Including correlations by increasing Λ rapidly corrects for this behavior. However, because the exact wave function is already localized around the 0p-0h configuration, and is contained within a few number of basis states, the effective wave function quickly converges towards the result characterized by $\beta = 0$ (see Table II). Thus, it appears that, near the phase transition, the full-space and truncated-space wave functions have comparable support, i.e., the number of basis states spanning these two wave functions is of the same order, and in that sense, there is no separation of scales to utilize.

B. Convergence of effective-model-space calculations with Λ and N

Figure 10 shows the difference between the energy of the exact ground state and the state in the effective model space

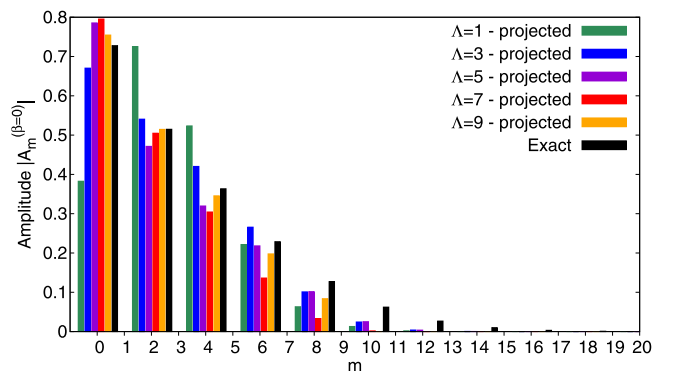


FIG. 9. Absolute value of the amplitudes $A_m^{(\beta=0)}$ in the effective wave function [see Eq. (14)], obtained for $N = 30$, $\bar{v} = 1.2$, and different cutoff values.

TABLE II. Values of the angle β obtained for different values of the cutoff Λ , for a system of $N = 30$ particles, and $\bar{v} = 1.2$.

Λ	β
1	0.586
3	0.496
5	0.371
7	0.113
9	0.000

(plain circles),

$$\Delta E(\Lambda) = |E_{\text{ex}} - E(\Lambda)|, \quad (21)$$

obtained for $\bar{v} = 2.0$, and for particle numbers $N = 32$ (green), $N = 64$ (blue) and $N = 96$ (red). For comparison, $\Delta E(\Lambda)_{\beta=0}$ obtained for $\beta = 0$ (empty circles) is also shown. The latter exhibits a polynomial convergence of the energy with respect to the size of the model space. This behavior is consistent with the convergence of the Bures distance of the wave function in Fig. 7. Similarly, optimizing β also accelerates the convergence of the energy in a way that is consistent with exponential convergence, up to a certain value of Λ , after which $\Delta E(\Lambda)$ reaches a plateau, before merging with the $\beta = 0$ solution. This behavior can again be easily understood, since for large Λ the solution has to converge to the exact one with $\beta = 0$. Because of the faster convergence of $\Delta E(\Lambda)$ for small cutoffs, the plateau region is thus necessary to link the symmetry-broken $\beta \neq 0$ and symmetry-unbroken $\beta = 0$ phases. The full squares in Fig. 10 display the energy difference $\Delta E(\Lambda)_{\text{proj}} = |E_{\text{ex}} - E(\Lambda)_{\text{proj}}|$ obtained after projecting onto a state of good parity. The projection sustains the exponential convergence to larger values of Λ , and allows for an improvement in precision by several orders of magnitude.

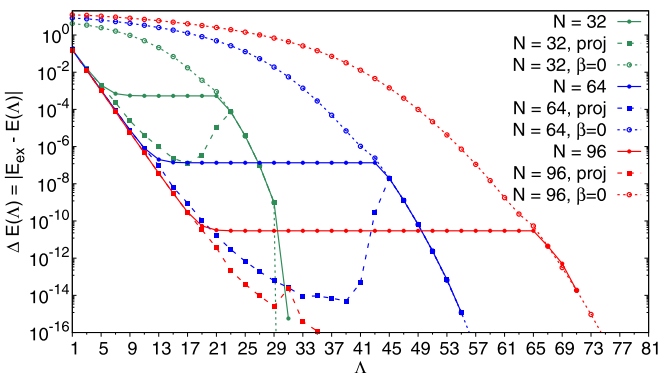


FIG. 10. The difference between the exact and effective model space ground-state energies $\Delta E(\Lambda)$ as a function of Λ for $\bar{v} = 2.0$ and for particle numbers $N = 32, 64$, and 96 . The plain circles and squares are the results obtained without and with projection onto a good-parity state, respectively. The empty circles show the results obtained when fixing $\beta = 0$ and increasing the model space. Numerical values for the shown results can be found in Tables X, XI, and XII.

Around $\Lambda \sim N/2$, the solution starts converging toward the $\beta = 0$ solution.³

IV. QUANTUM SIMULATIONS: GENERAL TECHNIQUES FOR HL-VQE

As discussed in earlier sections, the Hamiltonian in truncated effective model spaces generally contains parameters that are absent in the full Hilbert space, β , which relate full-space and effective-space ladder operators. There are stationary values of β that, when combined with an optimal wave function, minimize the total energy of the system. We therefore define the expectation value of the energy in the effective model space as a cost function to be minimized with respect to both the Hamiltonian parameters, β , and the parameters defining the wave function, which we will generally denote here as θ :

$$E(\beta, \theta) = \langle \psi(\theta) | \hat{H}(\beta) | \psi(\theta) \rangle. \quad (22)$$

Assuming uniquely isolated ground states, this minimization simultaneously learns the Hamiltonian in the effective model space and identifies the associated variational ground-state wave function. We define this to be the Hamiltonian learning variational quantum eigensolver (HL-VQE). A straightforward way to converge to the optimal parameter set (for non-pathological systems) is to use gradient descent, employing the linear variation of the $E(\beta, \theta)$. Combining the sets of parameters into $\mathbf{w} = (\beta, \theta)$, the iteration between adjacent parameter estimates is

$$\mathbf{w}^{[k+1]} = \mathbf{w}^{[k]} - \eta \nabla_{\mathbf{w}} E(\mathbf{w}^{[k]}), \quad (23)$$

where η is the learning rate. It is well known how to extend this beyond linear order to quadratic order, but we have not implemented this.⁴

Generally, the Hamiltonian in the effective model spaces can be expanded in terms of coefficients, that are function of β , times products of Pauli operators, as

$$\hat{H}(\beta) = \sum_{i_1, \dots, i_M=1}^4 h_{i_1, \dots, i_M}(\beta) \bar{\sigma}_{i_1} \otimes \dots \otimes \bar{\sigma}_{i_M}, \quad (24)$$

where $\bar{\sigma} = \{\hat{X}, \hat{Y}, \hat{Z}, \hat{I}\}$. The cost function in Eq. (22) becomes

$$E(\beta, \theta) = \sum_{i_1, \dots, i_M=1}^4 h_{i_1, \dots, i_M}(\beta) \times \langle \Psi(\theta) | \bar{\sigma}_{i_1} \otimes \dots \otimes \bar{\sigma}_{i_M} | \Psi(\theta) \rangle. \quad (25)$$

The HL-VQE requires the computation of the cost function $E(\beta, \theta)$, as well as its derivatives with respect to β and θ for

³For sufficiently large N and Λ , maintaining precision in the results of matrix diagonalizations for the energy difference shown in Fig. 10 becomes increasingly challenging.

⁴For the system sizes considered in this work, only the simplest classical implementation of gradient-descent methods is used. For simulations of larger spaces, more sophisticated algorithms will be necessary, such as ADAM [73] or ADAGRAD [74].

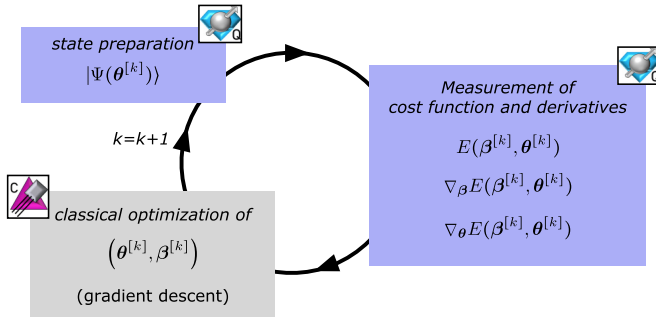


FIG. 11. A schematic of the workflow implementing the HL-VQE algorithm. The icons denoting classical or quantum computation are defined in Ref. [77].

the gradient descent. This involves computing the coefficients $h_{i_1, \dots, i_M}(\beta)$ and their derivatives with respect to β , as well as the expectation values of the Pauli operators $\langle \Psi(\theta) | \bar{\sigma}_{i_1} \otimes \dots \otimes \bar{\sigma}_{i_M} | \Psi(\theta) \rangle$ and their derivatives with respect to θ . Generally, and as we will assume for the analysis of the LMG model, the coefficients $h_{i_1, \dots, i_M}(\beta)$ and their derivatives can be evaluated classically. These classical computations become increasingly demanding with increasing dimensionality of the effective space(s). With the factorization in Eq. (25), it is therefore the expectation values of the strings of Pauli operators evaluated in the quantum-many-body wave function, as well as their derivatives with respect to θ , which will require quantum computation for a sufficiently large effective model space. The corresponding procedure for the LMG model⁵ is detailed in Sec. V.

Figure 11 summarizes the general workflow for HL-VQE.

- (i) An initial set of parameters $(\beta^{[0]}, \theta^{[0]})$ is chosen.
- (ii) The algorithm then starts with preparation of the state $|\Psi(\theta^{[0]})\rangle$ which can usually be implemented in many ways with quantum circuits. In Sec. V, we will choose quantum circuit structures such that each angle parametrizing the wave function appears only in one gate of the circuit. Thus, partial derivatives with respect to that angle are localized to that one gate and can be evaluated using a finite-difference relation. See Appendix B for more details.
- (iii) As is the case for VQE, matrix elements of strings of Pauli operators are appropriately transformed into the computational basis, where the polarization of each qubit in the register along the z basis is projected for each member of the ensemble. From these measurements, the expectation values of each operator can be evaluated.
- (iv) Classical computers are used to evaluate $\hat{H}(\beta^{[0]})$ and $\nabla_{\beta} \hat{H}(\beta^{[0]})$, so that the cost function $E(\beta^{[0]}, \theta^{[0]})$ and

its derivatives, $\nabla_{\theta} E(\beta^{[0]}, \theta^{[0]})$ and $\nabla_{\beta} E(\beta^{[0]}, \theta^{[0]})$, can be reconstructed classically, from the outputs of the quantum device.

- (v) Subsequently, a new set of parameters $(\beta^{[1]}, \theta^{[1]})$ is determined via classical optimization (here gradient descent, as described above).
- (vi) This procedure is repeated until the effective model space Hamiltonian, wave function, and cost function converge.

We note that similar ideas have been developed and applied in the fields of quantum chemistry and condensed matter. For instance, Ref. [78] introduced an algorithm for determining (nonvariational) natural orbitals, which was applied to the two-dimensional Hubbard model, and Refs. [56,57] developed orbital-optimized VQE (oo-VQE) techniques for molecular calculations, which optimize orbitals via a variational principle, closer to the spirit of our present work, but using a unitary coupled cluster (UCC) ansatz of the wave function. Contrarily to the present HL-VQE, where both the orbital parameters β (or, equivalently, the effective Hamiltonian) and the wave function parameters θ are determined simultaneously at each iteration, the orbital optimizations of Refs. [57,78] were, however, performed via two-step procedures, in which the orbitals are determined classically using the outputs of the VQE. While the algorithm developed of Ref. [56] involved a one-step process, it differs from ours in a number of ways. In particular, it employed a more costly fermion-to-qubit mapping, together with a UCC ansatz for the wave function which was further truncated in order to keep the number of wave function parameters polynomial.

While in this work we focus on the determination of the variational ground state, the HL-VQE algorithm described here can also be applied to the description of excited states, with few modifications. This is outlined in Appendix E. We also note that, although we consider Hamiltonian parameters corresponding to a one-body orbital transformation, the HL-VQE algorithm can also be applied to more general parameter learning, such as unitary transformations of the Hamiltonian generated by two-body (or three-body) operators, with obvious connections to similarity renormalization group (SRG) and in-medium SRG (IM-SRG) methods.

V. QUANTUM SIMULATIONS: IMPLEMENTING HL-VQE AND RESULTS FROM IBM'S QUANTUM COMPUTERS

In this section, HL-VQE is applied to the LMG model, for which the space of Hamiltonian parameters $\beta = \beta$ is one dimensional. We employ a form of the wave function $|\Psi\rangle^{(\Lambda)}$ given in Eq. (12), and present algorithms designed to be executed on IBM's QExperience quantum computers [53]. Results obtained for small quantum circuits using the simulator AER and quantum computer `ibm_lagos` are presented.

A. Mapping and state preparation

In order to implement the HL-VQE method on a digital quantum computer, an ansatz for the effective state $|\Psi\rangle^{(\Lambda)}$ that can be obtained by action of a unitary operator is required. In general, this is not obviously achievable when the state is

⁵In future generalizations of the HL-VQE algorithm to more realistic systems than the present LMG model, the use of recently developed techniques, such as classical shadows [75] and importance-sampled classical shadows [76], could potentially provide robust estimates of the expectation values with a reduced number of measurements.

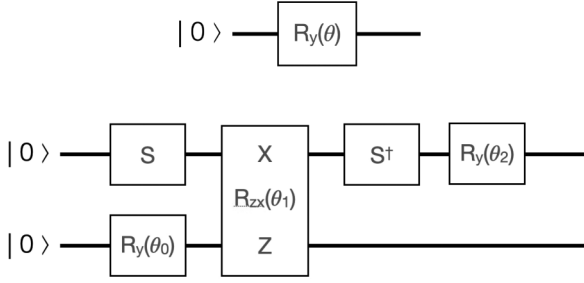


FIG. 12. Quantum circuits that can be used to prepare real wave functions on one (upper) and two (lower) qubits. The two-qubit circuit utilizes IBM's native $R_{ZX}(\theta)$ gate, and for clarity the orientation of the $\hat{X} \otimes \hat{Z}$ operation is shown explicitly.

written as a linear expansion of Slater determinants. In the case of the LMG model, this is, however, possible by adopting a mapping similar to the one used in quantum simulations of quantum field theories [79–82], where the many-body basis states (as opposed to the fermionic modes) are mapped onto the qubits. In that case the number of required qubits n_q is fixed by the desired cutoff as $\Lambda = 2^{n_q}$.

For a CP -conserving Hamiltonian, such as the bare or effective Hamiltonians $\hat{H}(\beta)$ of the LMG model, the wave function in the Hilbert space $|\Psi\rangle^{(\Lambda)}$ in Eq. (12) can be made relatively real, and, as such, there are $\Lambda - 1$ angles $\theta = \{\theta_i\}_{i=1, \dots, \Lambda-1}$ required to define the Λ amplitudes $\{A_n^{(\beta)}\}$ of the states (unitarity fixes the remaining amplitude). The parametrized state $|\Psi\rangle^{(\Lambda)}$ can then be obtained by action of a unitary operator $\hat{\mathcal{W}}(\theta)$, as $|\Psi\rangle^{(\Lambda)} \equiv |\Psi(\theta)\rangle^{(\Lambda)} = \hat{\mathcal{W}}(\theta)|n=0, \beta\rangle$. In practice, $|\Psi(\theta)\rangle^{(\Lambda)}$ can be prepared by initializing the quantum register in the computational-basis state $|\Psi\rangle_{\text{ini}} = |0\rangle^{\otimes N}$, corresponding to the unentangled 0p-0h configuration $|n=0, \beta\rangle$, and acting on the register with a quantum circuit involving $\Lambda - 1$ angles implementing $\hat{\mathcal{W}}(\theta)$. There are many ways to achieve this. As mentioned above, we designed circuits such that each angle θ_i appears only once in the gates comprising the circuit. In that way, partial derivatives of the cost function with respect to θ_i are localized to one operator. This will allow for any derivative with respect to the angles θ to be evaluated in the same way using a finite-difference relation, that does not suffer from unnecessarily large statistical uncertainties. This is discussed in more detail in Appendix B. The quantum circuits can be constructed in terms of the available quantum gate set associated with a particular quantum computer. We chose to work with IBM's QExperience superconducting quantum computers [53].

To provide elementary examples of the technique, we execute quantum simulations of effective model spaces with $\Lambda = 2, 4$, corresponding to one and two qubits, respectively, and as such do not consider generation of quantum circuits to furnish real wave functions in arbitrary-sized Hilbert spaces. Figure 12 displays the corresponding quantum circuits used to prepare arbitrary real wave functions. The two-qubit circuit uses IBM's native $R_{ZX}(\theta)$ gate. The use of this gate allows us to reduce the number of entangling operations. The wave functions that are prepared, when the circuits in Fig. 12 act on

the states $|0\rangle$ and $|00\rangle$ respectively, are

$$\begin{aligned} |\Psi(\theta)\rangle^{(2)} &= \cos \frac{\theta}{2} |0\rangle + \sin \frac{\theta}{2} |1\rangle, \\ |\Psi(\theta)\rangle^{(4)} &= \cos \frac{\theta_0}{2} \cos \frac{\theta_2 - \theta_1}{2} |00\rangle + \sin \frac{\theta_0}{2} \cos \frac{\theta_2 + \theta_1}{2} |10\rangle \\ &\quad + \cos \frac{\theta_0}{2} \sin \frac{\theta_2 - \theta_1}{2} |01\rangle + \sin \frac{\theta_0}{2} \sin \frac{\theta_2 + \theta_1}{2} |11\rangle. \end{aligned} \quad (26)$$

These correspond to the ansatz in Eq. (12) for the wave function, with the mapping

$$\begin{aligned} |0\rangle &\equiv |n=0, \beta\rangle, \\ |1\rangle &\equiv |n=1, \beta\rangle, \end{aligned} \quad (27)$$

for the one-qubit case, and

$$\begin{aligned} |00\rangle &\equiv |n=0, \beta\rangle, \\ |01\rangle &\equiv |n=1, \beta\rangle, \\ |10\rangle &\equiv |n=2, \beta\rangle, \\ |11\rangle &\equiv |n=3, \beta\rangle, \end{aligned} \quad (28)$$

for the two-qubit case.

B. Quantum computation of the expectation values and derivatives

Once the state in the effective model state $|\Psi(\theta)\rangle^{(\Lambda)}$ has been prepared, the cost function $E(\beta, \theta)$ and its derivatives with respect to β and θ can be computed.

The two-dimensional effective model space that can be mapped onto one qubit has a Hamiltonian expectation value and β derivative of the form, when given in terms of Pauli operators,

$$\begin{aligned} \langle \hat{H}^{(2)}(\beta) \rangle &= -\frac{N-1}{4} [(N-3)V \sin^2 \beta + 2\varepsilon \cos \beta] \langle \hat{I} \rangle \\ &\quad - \frac{1}{4} [3(N-1)V \sin^2 \beta + 2\varepsilon \cos \beta] \langle \hat{Z} \rangle \\ &\quad + \frac{\sqrt{N}}{2} [\varepsilon - (N-1)V \cos \beta] \sin \beta \langle \hat{X} \rangle, \\ \nabla_{\beta} \langle \hat{H}^{(2)}(\beta) \rangle &= \frac{N-1}{2} [\varepsilon - (N-3)V \cos \beta] \sin \beta \langle \hat{I} \rangle \\ &\quad + \frac{1}{2} [\varepsilon - 3(N-1)V \cos \beta] \sin \beta \langle \hat{Z} \rangle \\ &\quad + \frac{\sqrt{N}}{2} [\varepsilon \cos \beta - (N-1)V \cos 2\beta] \langle \hat{X} \rangle, \\ \nabla_{\theta} \langle \hat{H}^{(2)}(\beta) \rangle &= -\frac{N-1}{4} [(N-3)V \sin^2 \beta + 2\varepsilon \cos \beta] \nabla_{\theta} \langle \hat{I} \rangle \\ &\quad - \frac{1}{4} [3(N-1)V \sin^2 \beta + 2\varepsilon \cos \beta] \nabla_{\theta} \langle \hat{Z} \rangle \\ &\quad + \frac{\sqrt{N}}{2} [\varepsilon - (N-1)V \cos \beta] \sin \beta \nabla_{\theta} \langle \hat{X} \rangle, \end{aligned} \quad (29)$$

where $\langle \hat{O} \rangle \equiv {}^{(2)}\langle \Psi(\boldsymbol{\theta}) | \hat{O} | \Psi(\boldsymbol{\theta}) \rangle^{(2)}$. Matrix elements of \hat{Z} are found from the difference of probabilities in the computational basis, while matrix elements of \hat{X} require further action by a Hadamard-gate \hat{H} prior to measurement. Derivatives of the expectation values of the Pauli operators with respect to $\boldsymbol{\theta}$, which are computed using the finite difference method, require two additional circuits per operator. Therefore six different ensembles of quantum circuits are needed. More details are provided in Appendix B 1.

For the two-qubit systems, the four-dimensional Hamiltonian in the $\Lambda = 4$ effective model space has a Pauli decomposition of the form

$$\begin{aligned} H^{(4)}(\beta) = & h_{II}^{(4)}(\beta) + h_{xx}^{(4)}(\beta) \hat{X} \otimes \hat{X} \\ & + h_{xz}^{(4)}(\beta) \hat{X} \otimes \hat{Z} + h_{xl}^{(4)}(\beta) \hat{X} \otimes \hat{I} \\ & + h_{yy}^{(4)}(\beta) \hat{Y} \otimes \hat{Y} + h_{zx}^{(4)}(\beta) \hat{Z} \otimes \hat{X} \\ & + h_{zz}^{(4)}(\beta) \hat{Z} \otimes \hat{Z} + h_{zl}^{(4)}(\beta) \hat{Z} \otimes \hat{I} \\ & + h_{lx}^{(4)}(\beta) \hat{I} \otimes \hat{X} + h_{lz}^{(4)}(\beta) \hat{I} \otimes \hat{Z}, \end{aligned} \quad (30)$$

with

$$\begin{aligned} h_{II}^{(4)}(\beta) &= \frac{1}{4}(N-3)[(N-7)V \sin^2(\beta) - 2\varepsilon \cos(\beta)], \\ h_{xx}^{(4)}(\beta) &= \frac{\sqrt{N-1} \sin(\beta)[\varepsilon + (N-3)V \cos(\beta)]}{2\sqrt{2}}, \\ h_{xz}^{(4)}(\beta) &= \frac{(\sqrt{N} - \sqrt{3}\sqrt{N-2})\sqrt{N-1}V[\cos(2\beta) + 3]}{8\sqrt{2}}, \\ h_{xl}^{(4)}(\beta) &= \frac{(\sqrt{N} + \sqrt{3}\sqrt{N-2})\sqrt{N-1}V[\cos(2\beta) + 3]}{8\sqrt{2}}, \\ h_{yy}^{(4)}(\beta) &= h_{xx}^{(4)}(\beta), \\ h_{zx}^{(4)}(\beta) &= \frac{1}{4} \sin(\beta)[\varepsilon(\sqrt{N} - \sqrt{3}\sqrt{N-2}) \\ &+ (N^{3/2} - \sqrt{3}\sqrt{N-2}N - \sqrt{N} \\ &+ 5\sqrt{3}\sqrt{N-2})V \cos(\beta)], \\ h_{zz}^{(4)}(\beta) &= \frac{3}{2}V \sin^2(\beta), \\ h_{zl}^{(4)}(\beta) &= \frac{3}{2}(N-3)V \sin^2(\beta) - \varepsilon \cos(\beta), \\ h_{lx}^{(4)}(\beta) &= \frac{1}{4} \sin(\beta)[\varepsilon(\sqrt{N} + \sqrt{3}\sqrt{N-2}) \\ &+ (N^{3/2} + \sqrt{3}\sqrt{N-2}N \\ &- \sqrt{N} - 5\sqrt{3}\sqrt{N-2})V \cos(\beta)], \\ h_{lz}^{(4)}(\beta) &= \frac{1}{4}[3(N-3)V \sin^2(\beta) - 2\varepsilon \cos(\beta)], \end{aligned} \quad (31)$$

with derivatives with respect to β that can be evaluated straightforwardly. The explicit forms for the expectation values of $H^{(4)}(\beta)$ are given in Eqs. (B12) and (B13) with products of Pauli operators \hat{I} , \hat{X} , \hat{Y} , or \hat{Z} acting on each qubit. For qubits with an \hat{X} the action of \hat{H} is further required, while for \hat{Y} the action of $\hat{S}^\dagger \hat{H}$ is required prior to measurement. For each operator, there are six additional circuits per operator

to provide derivatives for the three angles θ_0 , θ_1 , and θ_2 , leading to 35 physics ensemble measurements per iteration step. Further details can be found in Appendix B 2.

With multiple circuits per iteration step, and using IBM's seven-qubit quantum computers, we explored packing multiple circuits for parallel running. For the one-qubit case, executing single-qubit jobs was found to minimize errors, but at the expense of an increased number of shots. For two-qubit circuits, the large number of ensemble measurements motivated executing multiple circuits in parallel. For each operator, we executed 1,2,2,2 circuits per job. After initial tuning, runs with 8 k shots per ensemble, where k denotes $\times 10^3$, we used 32 k shots per circuit in production on `ibm_lagos`. We used 100 k shots per circuit on the AER classical simulator. IBM's measurement error correction routine was used as part of postprocessing, and, because of the shallow circuit depth and the use of the R_{ZX} gate, we did not utilize a CNOT extrapolation [83,84] or randomized compiling of the CNOTs (Pauli twirling) [85], and we also did not use dynamic decoupling [86–89] or decoherence renormalization [90–92].⁶

C. Gradient descent and workflow of the calculation

For a given iteration $[k]$ of the procedure, once the numerical values of

$$\begin{aligned} G_\beta^{[k]} &= {}^{(\Lambda)}\langle \Psi(\boldsymbol{\theta}^{[k]} | \nabla_\beta \hat{H}(\beta^{[k]} | \Psi(\boldsymbol{\theta}^{[k]}))^{(\Lambda)}, \\ G_\theta^{[k]} &= \nabla_\theta {}^{(\Lambda)}\langle \Psi(\boldsymbol{\theta}^{[k]} | \hat{H}(\beta^{[k]} | \Psi(\boldsymbol{\theta}^{[k]}))^{(\Lambda)} \end{aligned} \quad (32)$$

have been determined from combined contributions from the classical and quantum computers, the values of the variational parameters at the next iterative step are determined using gradient descent,

$$\begin{aligned} \beta^{[k+1]} &= \beta^{[k]} - \eta G_\beta^{[k]} / \mathcal{G}^{[k]}, \\ \boldsymbol{\theta}^{[k+1]} &= \boldsymbol{\theta}^{[k]} - \eta G_\theta^{[k]} / \mathcal{G}^{[k]}, \\ \mathcal{G}^{[k]} &= \sqrt{|G_\beta^{[k]}|^2 + |G_\theta^{[k]}|^2}, \end{aligned} \quad (33)$$

where η is the learning rate. Tuning led to setting $\eta = 0.07$ for production using one and two qubits with Eq. (33). What we have described above is slightly different from what can be found in Appendix B and Eq. (23) in defining the update step, but was found to lead to more rapid numerical convergence. The iteration continues until the wave function amplitudes and ground-state energy stabilize, or until the number of iterations reaches a given value, a number exceeding $N_{\text{iter}} \geq 80$.

D. Results for one-qubit truncation: $\Lambda = 2$

For our production using IBM's QExperience superconducting quantum computer `ibm_lagos` and the simulator AER, one set of model parameters was used: $N = 30$, $\bar{v} = V(N-1)/\varepsilon = 2.0$, and $\varepsilon = 1.0$. These parameters will allow for a comparison with the results obtained with explicit diagonalizations that were presented in Sec. III. The quantum

⁶Studies of the stability of (some of) IBM's quantum computers can be found in Ref. [93].

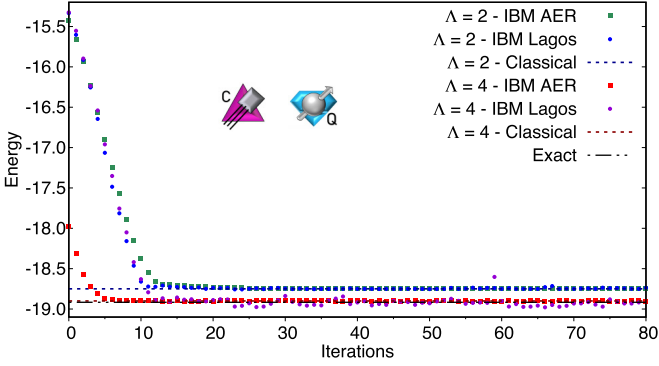


FIG. 13. Central values of the ground-state energies (in units of ε) obtained for the $\Lambda = 2, 4$ systems from one- and two-qubit simulations using AER and `ibm_lagos` for the LMG-model parameters using 100 k and 32 k shots, respectively. Numerical values for these energies are given in Tables V and VI. The starting values of variational parameters of the one-qubit simulations were $\beta^{[0]} = 0.2$ and $\theta_i^{[0]} = 0.30$ using AER and $\beta^{[0]} = 0.2$ and $\theta_i^{[0]} = 0.10$ using `ibm_lagos`. The starting values of variational parameters of the two-qubit simulations were $\beta^{[0]} = 0.8$ and $\theta_i^{[0]} = 0$ using AER, and $\beta^{[0]} = 0.2$ and $\theta_i^{[0]} = 0$ using `ibm_lagos`. The dark blue and dark red dashed lines show the results obtained from exact diagonalization in the effective model spaces $\Lambda = 2$ and $\Lambda = 4$, respectively. The black dotted-dashed line shows the exact result, obtained from exact diagonalization in the full Hilbert space.

circuits, HL-VQE algorithm, and workflow described above were implemented using a learning rate of $\eta = 0.07$ and starting values of the parameters $\beta^{[0]} = 0.2$ and $\theta_i^{[0]} = 0.10$. Typically, 80 iterations were performed, with stable results being obtained after many fewer.

The results obtained from `ibm_lagos` and AER for the central values of the ground-state energy (in unit of ε) as a function of iteration are shown in Fig. 13, and numerical values are given in Tables V and VI. The uncertainty associated with each iteration is not shown, but can be deduced, in combination with other uncertainties, from the fluctuations about the mean value (as each iteration is statistically independent). The ground-state energy of the $\Lambda = 2$ systems obtained from AER and `ibm_lagos` are consistent with each other, and with the exact diagonalization in the (truncated) effective model space performed in Sec. III (see Table III). As different starting values of parameters in the HL-VQE were used in production on AER and `ibm_lagos`, a direct and meaningful comparison of the two approaches to the ground-state energy should not be made, and only the asymptotic values and uncertainties should be compared.

The wave function amplitudes as a function of iteration are shown in Fig. 14 and numerical values are given in Tables V and VI. For an effective model space with $\Lambda = 2$ states, the effective Hamiltonian is defined by the lowest-lying 2×2 block of $H(\beta)^{(2)}$. Thus, for fixed values of N , ε and \bar{v} , it is a 2×2 numerical matrix with entries that are functions of β . For the value of \bar{v} we are considering, the structure of the Hamiltonian is such that the vanishing of the off-diagonal element, $\Xi = \varepsilon - (N - 1)V \cos \beta = 0$, corresponds to the minimum of the lowest-lying eigenvalue. This is most

TABLE III. Results obtained for $N = 30$, $\varepsilon = 1.0$, and $\bar{v} = 2.0$ using IBM's AER and `ibm_lagos`, and results obtained by exact diagonalization, in the $\Lambda = 2$ effective model space and in the full Hilbert space. The central values and uncertainties are derived from iterations steps between 70 and 80. The central value is the mean in this interval, while the uncertainty is the half the difference between the maximum and minimum values. The values at each iteration step from which these results are obtained, are given in Tables V and VI, and displayed in Figs. 13, 14, and 16.

Quantity	AER	<code>ibm_lagos</code>	Exact effective	Exact full
$E_{g.s.}$	-18.7500(0)	-18.7490(37)	-18.750000	-18.916414
β	1.0472(14)	1.041(13)	1.0471975	0
$ A_0 $	1.00000(2)	1.00000(5)	1	
$ A_1 $	0.0018(12)	0.0035(16)	0	
D_B	0.1926(7)	0.1922(15)	0.1922023	

easily seen in an N -expansion followed by a considerations of perturbations around $\Xi = 0$. In that case the ground state of this system corresponds to $|\Psi(\theta)\rangle^{(2)}$ in Eq. (26) with $\theta = 0$, and therefore is without mixing between 0p-0h and 1p-1h configurations in the truncated basis, corresponding to the HF state. See Appendix C for more details. We see from Fig. 14 that the amplitudes obtained from both AER and `ibm_lagos` are consistent with these expectations, as we observe that the amplitude of the 1p-1h state is systematically decreasing with iteration steps. The precision of extracted amplitudes, at any iteration step, is limited by the precision used in the workflow, along with the learning rate. The results obtained with `ibm_lagos` show signs of the impact of simulation errors at the percent level, as is to be expected, with similar fluctuations occurring an order of magnitude smaller for AER. The convergence to the known result is consistent with an exponential over a large number of iteration steps.

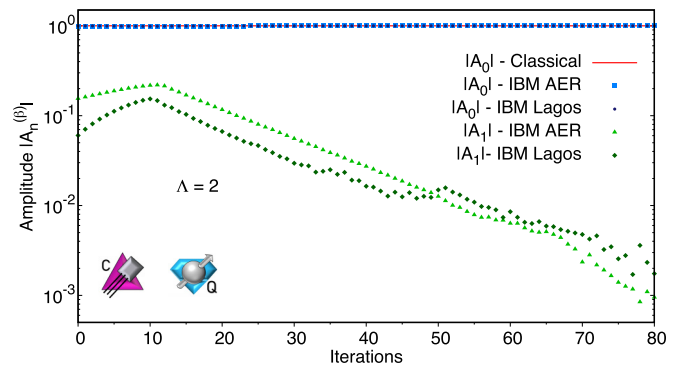


FIG. 14. Central values of the wave function amplitudes obtained for the $\Lambda = 2$ systems from one-qubit simulations using AER and `ibm_lagos` for the LMG-model parameters using 100 k and 32 k shots, respectively. Numerical values for these amplitudes are given in Tables V and VI. The starting values of variational parameters of the one-qubit simulations were $\beta^{[0]} = 0.2$ and $\theta_i^{[0]} = 0.30$ using AER and $\beta^{[0]} = 0.2$ and $\theta_i^{[0]} = 0.10$ using `ibm_lagos`. Exact diagonalization in the effective model space yields $|A_0| = 1$ (red horizontal line) and $|A_1| = 0$.

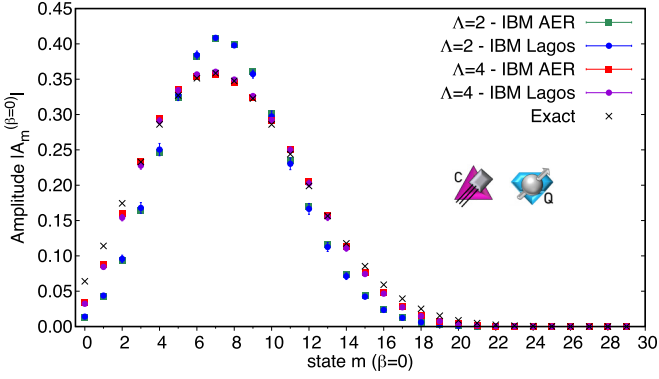


FIG. 15. Full-space wave functions reconstructed from the effective model spaces with $\Lambda = 2, 4$ from one- and two-qubit simulations using AER and `ibm_lagos` for the LMG-model parameters using 100k and 32k shots, respectively. The black crosses denote the exact full-Hilbert space wave functions. Numerical values for these amplitudes are given in Table IX. The starting values of variational parameters of the one-qubit simulations were $\beta^{[0]} = 0.2$ and $\theta_i^{[0]} = 0.30$ using AER and $\beta^{[0]} = 0.2$ and $\theta_i^{[0]} = 0.10$ using `ibm_lagos`. The starting values of variational parameters of the two-qubit simulations were $\beta^{[0]} = 0.8$ and $\theta_i^{[0]} = 0$ using AER, and $\beta^{[0]} = 0.2$ and $\theta_i^{[0]} = 0$ using `ibm_lagos`. The uncertainties are determined from the standard deviation derived from a correlated propagation of the last 20 iterations.

The full-space wave functions (expressed in the unrotated $\beta = 0$ basis) reconstructed from the previous $\Lambda = 2$ effective model space using Eq. (17) are shown in Fig. 15 (green and blue points), with numerical results given in Table IX. The Bures distance of the reconstructed full-space wave function, given in Eq. (19), is displayed in Fig. 16. While the convergence of the amplitudes and energies towards the expected

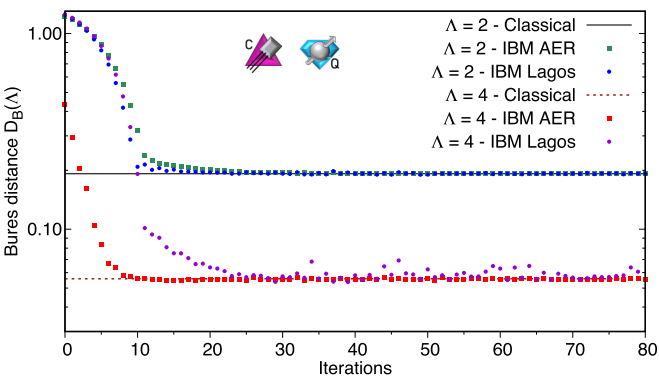


FIG. 16. Central values of the Bures distance defined in Eq. (19), obtained for the $\Lambda = 2, 4$ systems from one- and two-qubit simulations using AER and `ibm_lagos` for the LMG-model parameters using 100 k and 32 k shots, respectively. Numerical values for these distances are given in Tables V and VI. The starting values of variational parameters of the one-qubit simulations were $\beta^{[0]} = 0.2$ and $\theta_i^{[0]} = 0.30$ using AER and $\beta^{[0]} = 0.2$ and $\theta_i^{[0]} = 0.10$ using `ibm_lagos`. The starting values of variational parameters of the two-qubit simulations were $\beta^{[0]} = 0.8$ and $\theta_i^{[0]} = 0$ using AER and $\beta^{[0]} = 0.2$ and $\theta_i^{[0]} = 0$ using `ibm_lagos`.

TABLE IV. Results obtained for $N = 30$, $\varepsilon = 1.0$, and $\bar{v} = 2.0$ using IBM's AER and `ibm_lagos`, and results obtained by exact diagonalization, from the $\Lambda = 4$ effective model space and in the full Hilbert space. The central values and uncertainties are derived from iterations steps between 70 and 80. The central value is the mean in this interval, while the uncertainty is the half the difference between the maximum and minimum values. The values at each iteration step from which these results are obtained, are given in Tables VII and VIII, and displayed in Figs. 13, 14, and 16.

Quantity	AER	<code>ibm_lagos</code>	Exact effective	Exact full
$E_{g.s.}$	-18.9000(12)	-18.929(44)	-18.900130	-18.916414
β	1.01479(39)	1.0160(96)	1.0162245	0
$ A_0\rangle$	0.98500(02)	0.98666(85)	0.98516	
$ A_1\rangle$	0.04193(18)	0.0469(98)	0.03901	
$ A_2\rangle$	0.16739(06)	0.1557(34)	0.16711	
$ A_3\rangle$	0.00020(01)	0.00258(28)	0	
D_B	0.05559(12)	0.0579(42)	0.05578	

(classical) values are consistent with single exponentials, the convergence of the $\Lambda = 2$ ground-state wave function has a different functional form, with initial fidelities only slowly converging for a number of iteration steps. This is followed by an interval of rapid convergence to the wave function that is exact for the effective model space.

A summary of the results obtained for the $\Lambda = 2$ state effective model space from IBM's classical simulator AER and from their superconducting-qubit quantum computer `ibm_lagos`, along with results obtained by exact diagonalization, in effective and full model spaces, are given in Table III. Good agreement is found between the results obtained from AER and `ibm_lagos`, and those from exact diagonalizations within the model space.

E. Results for two-qubit truncation: $\Lambda = 4$

The HL-VQE algorithm is applied to the $\Lambda = 4$ system in the same way that it was applied to the $\Lambda = 2$ system, with the obtained ground-state energy as a function of iteration shown in Fig. 13 (red and purple points), with a converged value provided in Table IV. The results obtained with both AER and `ibm_lagos` are consistent with the exact value in the effective model space, but the results from AER are an order of magnitude more precise than that from `ibm_lagos`. The extracted value of β from AER is a few standard deviations away from the expected value, while that from `ibm_lagos` is consistent, but with a larger uncertainty, as seen in Table IV.

Figure 17 shows the amplitudes $|A_n^{(\beta)}|$ of the $\Lambda = 4$ states in the effective model space determined with AER and `ibm_lagos`. With the effective Hamiltonian $H^{(4)}(\beta)$ [see Eq. (30)] truncated for $\Lambda = 4$ states, and with the parameters used in the $\Lambda = 4$ effective model space, the amplitude of the 3p-3h state is expected to vanish by the arguments given in Appendix C 2. However, this expectation was not enforced in carrying out the HL-VQE, and, in addition to β , the three angles θ_0 , θ_1 , and θ_2 , in $|\Psi(\theta)\rangle^{(4)}$ [Eq. (26)] were varied. The amplitude of the 3p-3h state is found to be much smaller than the other amplitudes from both simulations, consistent with its

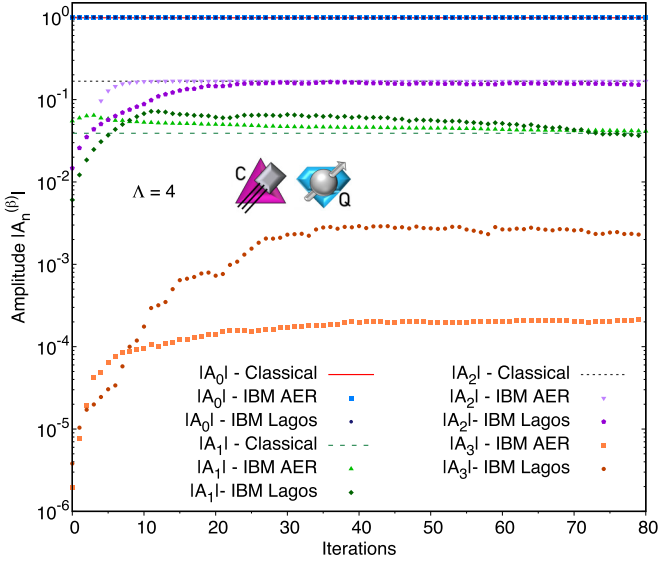


FIG. 17. Central values of the wave function amplitudes obtained for the $\Lambda = 4$ systems from two-qubit simulations using AER and `ibm_lagos` for the LMG-model parameters using 100 k and 32 k shots, respectively. Numerical values for these amplitudes are given in Tables VII and VIII. The starting values of variational parameters of the two-qubit simulations were $\beta^{[0]} = 0.8$ and $\theta_i^{[0]} = 0$ using AER and $\beta^{[0]} = 0.2$ and $\theta_i^{[0]} = 0$ using `ibm_lagos`. Exact diagonalization in the truncated effective space yields the values of $|A_0|$, $|A_1|$, and $|A_2|$, shown with horizontal lines, and $|A_3| = 0$.

vanishing in the exact diagonalization in the effective model space, along with the statistical and systematic errors implicit in the simulations. The results obtained for $|A_{0,1,2,3}^{(\beta)}|$ from AER and `ibm_lagos` at large iteration number are consistent with each other and with expectations at the few- σ level, as can be seen from Fig. 17 and Tables IV, VII, and VIII.

The full-space wave functions reconstructed from $|A_{0,1,2,3}^{(\beta)}|$ using Eqs. (16) and (17) are shown in Fig. 15 (red and purple points) and given in Table IX. The corresponding Bures distance to the exact full-space wave function is shown in Fig. 16 and given in Tables VII and VIII. The Bures distance for $\Lambda = 4$ is significantly improved over that for $\Lambda = 2$, consistent with the exponential scaling for $\Lambda \ll N$ that is anticipated from the exact calculations in effective model space.

F. The scaling of quantum resources

It is helpful to consider the scaling of quantum resources required for these effective model space simulations in order to estimate the practicality of our HL-VQE algorithm. For the present calculations using `ibm_lagos`, the workflow that we implemented for $\Lambda = 4$ used 1,2,2,2 circuits per ensemble run, with 32k shots (measurements) per ensemble, for a total of 128k shots. For the 80 iterations that were run, this corresponds to $\approx 10.2 \times 10^6$ shots. Of course, this number could be reduced using more sophisticated classical search algorithms, implementing more aggressive convergence criteria, implementing a dynamical shot estimator between iterations, and more, but the order-of-magnitude quantum resource cost will remain.

The exponential growth in the number of angles required to define the variational wave function, scaling with the number of states in the Hilbert space, nominally renders VQE algorithms unsuitable for use at scale. However, with the double exponential improvement in ground-state energy and wave function fidelity with increasing number of qubits supporting the effective model spaces for $\Lambda \ll N$, the scaling of the VQE algorithm, and in this case the HL-VQE algorithm, becomes favorable for increasing the size of effective model spaces until threshold effects become significant.

VI. SUMMARY, CONCLUSIONS, AND OUTLOOK

We have performed a detailed study of the use of effective model spaces and effective Hamiltonians for the preparation of low-lying states of the Lipkin-Meshkov-Glick model, a well-known solvable nuclear physics model of multi-nucleon systems, using quantum computers. In this model, while variational ground states for systematically truncated Hamiltonians exhibit power-law convergence to the exact results, additionally optimizing the truncated Hamiltonian from a variational principle is shown to exponentially improve convergence throughout the regime where the optimal energy surface leads to spontaneous symmetry breaking. We have demonstrated these gains using exact and approximate classical calculations. These findings indicate that quantum simulations using small model spaces with variationally improved Hamiltonians can furnish precise and accurate results, and have utility in bounded-error simulations with reduced quantum resource requirements. Borrowing ideas from quantum chemistry, we have suggested and explored an algorithm that combined Hamiltonian learning with VQE to be used in classical-quantum hybrid computing environments, which we call HL-VQE. In this algorithm, parameters defining an effective Hamiltonian used in an effective model space (or EFT), and the parameters defining its ground-state wave function, are simultaneously determined through minimization of an associated cost function, which we took to be the ground-state energy. In the regime where the convergence is scaling exponentially with increasing model space dimensionality because of the localized wave function in the Hilbert space, the HL-VQE algorithm is efficient, with the addition of a single qubit, and associated state preparation resource requirements, leading to an exponential improvement in ground-state energy and wave function fidelity, compared to traditional VQE. This was demonstrated by classical calculations and by performing quantum simulations of one- and two-qubit systems using IBM's simulator and quantum computer, AER and `ibm_lagos`, which reproduced the expected classical results within (small) uncertainties.

There are obvious connections and differences between this work and unitary coupled-clusters calculations of the LMG model. The HL-VQE algorithm involves performing a unitary transformation on the states, mixing particle-hole states, which leads to a unitary-equivalent Hamiltonian. In addition to limiting the form of the transformation, the Hilbert space is truncated and the Hamiltonian optimized in the truncated space. To add some further context to the HL-VQE method, while the previous coupled-cluster simulations of

systems of N particles required N qubits, the HL-VQE method requires $\log \Lambda$, and so a LMG model with $N \approx 100$, which is generically impractical today for the coupled-cluster VQE algorithms, can be simulated with exponential precision with just two or three qubits using HL-VQE. In some ways, HL-VQE makes a bridge between coupled-cluster expansions and EFT techniques. It is conceivable that a combination of ADAPT-VQE and HL-VQE algorithms could also be useful due to their complementary nature. Exploring and better understanding these connections, similarities, and differences is the subject of future works.

This study of the Lipkin-Meshkov-Glick model has provided insights and demonstrations of the utility of Hamiltonian learning in effective model spaces. As this model exhibits symmetries of simple and well-structured interactions, the question remains as to the utility beyond this model for more realistic effective interactions. We do not address this question in this work; however, we find it likely that for systems where there are clear separations of scale(s), some or all of the methods developed and employed in this work can also be used, and will be the subject of future work. An important element of this framework is that the optimal value of the variational parameter in the Hamiltonian is such that, in the transformed basis, the multi-particle-hole correlations are strongly localized around the mean-field (Op-Oh) solution, and rapidly converge with increasing model space.

In general, the noncommutativity of the global orbital transformation with the truncation to effective model spaces is the feature that provides an opportunity for variational improvements through Hamiltonian learning. This is one unitary transformation that rearranges matrix elements and entanglement in nuclear many-body systems. Another such unitary transformation is the SRG, in which a flow that, in its simplest form, introduces a Gaussian suppression of high momentum modes in the system. Consequently, the Hamiltonian matrix is evolved toward a block diagonal form. While somewhat dissimilar in form, the SRG flow and a truncation do not generally commute, and the utility for SRG-flowed systems remains to be explored. Similarly, the HL-VQE algorithm, used together with a desired ansatz for the nuclear state, could be potentially utilized to perform various versions of in-medium SRG (IMSRG) on a quantum computer. A further possibility that comes to mind, would be to use the variational orbital transformation, which reduces the coupling between effective model space and the remaining part of the Hilbert space [33], as a preprocessing step before the IMSRG procedure.

The HL-VQE algorithm combined with the use of effective model spaces is likely to have applicability beyond nuclear many-body systems. EFTs are a well-defined and systematic ways to recover S -matrix elements and bound states from a (more) complete theory through operator and Hamiltonian matching or through reproducing experimental results. As such, variationally optimizing nonperturbative leading-order contributions, when the one-body and higher-body interactions make comparable contributions, though the HL-VQE algorithm may have applicability to EFT calculations of few-body systems. It could also be the case that these methods will be useful in simulating quantum field theories, e.g.,

Refs. [13,94], in particular, lattice scalar field theory and gauge theories. For example, local truncations in the representations of the $SU(N_c)$ in each link space could be mitigated by improving the Kogut-Susskind Hamiltonian [95] and learning the coefficients of gauge-invariant operators. A challenge for this application is to transform the states in the local Hilbert spaces in such a way to preserve Gauss's law at each vertex, e.g., Refs. [96], or to include protocols that constrain the wave function to the gauge-invariant space. In addition, the methods developed in this work may also be useful in designing quantum sensors, where VQE is being utilized in encoding and decoding sensors to enhance sensitivity to external fields [97]. These applications are the subject of future work.

The part of this paper that has focused on quantum simulation has addressed implementations using digital devices. With the rapid convergence with increasing dimension of the effective model space, it is useful to consider implementations on other devices such as analog simulators and quantum annealers. For the $\Lambda = 2, 4$ systems that we have considered, and for much larger effective model spaces, analogous calculations could be performed using, for example, D-Wave's quantum annealers, such as ADVANTAGE [98]. This too will be the subject of future work.

In closing, with the approximate symmetries of QCD and the emergent separations of scales, which in some sense define nuclear physics, implementing the HL-VQE algorithm in low-energy effective model spaces using quantum computers may have utility for calculations involving realistic nuclear forces, and also for improving convergence of quantum simulations of quantum field theories relevant to the standard model.

ACKNOWLEDGMENTS

We would like to thank Anthony Ciavarella, Jon Engel, and Marc Illa for helpful discussions, and for all of our other colleagues and collaborators that provide the platform from which this work has emerged. Caroline Robin would like to thank the Inqubator for Quantum Simulation (IQuS) at the University of Washington for kind hospitality during this work. This work was supported, in part, by Universität Bielefeld and ERC-885281-KILONOVA Advanced Grant, and, in part, by the U.S. Department of Energy, Office of Science, Office of Nuclear Physics, Inqubator for Quantum Simulation (IQuS) under Award No. DOE (NP) DE-SC0020970. We acknowledge the use of IBM Quantum services for this work. The views expressed are those of the authors, and do not reflect the official policy or position of IBM or the IBM Quantum team. It was enabled, in part, by the use of advanced computational, storage, and networking infrastructure provided by the Hyak supercomputer system at the University of Washington [99] and was also supported, in part, through the Department of Physics [100] and the College of Arts and Sciences [101] at the University of Washington.

APPENDIX A: THE LIPKIN-MESHKOV-GLICK MODEL: MORE DETAILS

In this Appendix, we provide more details about computing matrix elements of the effective Hamiltonian in the LMG

model. The Hamiltonian can be written as

$$\hat{H} = \varepsilon \hat{J}_z - \frac{V}{2}(\hat{J}_+^2 + \hat{J}_-^2), \quad (\text{A1})$$

where the quasispin operators \hat{J} are defined in Eq. (2). A rotation by an angle β around the y axis,

$$\hat{J} \equiv \hat{J}(\beta = 0) \mapsto \hat{J}(\beta), \quad (\text{A2})$$

in quasispin space can be obtained from the general transformation properties of rank-1 spherical tensors

$$\begin{aligned} T_q^{(1)}(\beta) &= \hat{U}^\dagger(\beta) \hat{T}_q^{(1)} \hat{U}(\beta), \\ &= \sum_{q'=0,\pm} d_{qq'}^1(\beta) \hat{T}_{q'}^{(1)}, \end{aligned} \quad (\text{A3})$$

where the spherical components are related via $\hat{J}_z = \hat{T}_0^{(1)}$, $\hat{J}_\pm = \pm\sqrt{2}\hat{T}_\pm^{(1)}$, and the expression for $d_{qq'}^1(\beta)$ is given in Eq. (17). This leads to

$$\hat{J}_z = \cos(\beta)J_z(\beta) + \frac{1}{2}\sin\beta[J_+(\beta) + J_-(\beta)], \quad (\text{A4})$$

$$\begin{aligned} \hat{J}_+ &= \frac{1}{2}[-2\sin(\beta)J_z(\beta) \\ &\quad + (\cos\beta + 1)J_+(\beta) + (\cos\beta - 1)J_-(\beta)], \end{aligned} \quad (\text{A5})$$

$$\begin{aligned} \hat{J}_- &= (J_+)^{\dagger} = \frac{1}{2}[-2\sin\beta J_z(\beta) \\ &\quad + (\cos\beta + 1)J_-(\beta) + (\cos\beta - 1)J_+(\beta)], \end{aligned} \quad (\text{A6})$$

corresponding to

$$\hat{J}_z(\beta) = \frac{1}{2} \sum_{p\sigma} \sigma c(\beta)_{p\sigma}^{\dagger} c(\beta)_{p\sigma}, \quad (\text{A7})$$

$$\hat{J}_+(\beta) = \sum_p c(\beta)_{p+}^{\dagger} c(\beta)_{p-}, \quad (\text{A8})$$

$$\hat{J}_-(\beta) = (\hat{J}_+)^{\dagger} = \sum_p c(\beta)_{p-}^{\dagger} c(\beta)_{p+}, \quad (\text{A9})$$

where the operators $c(\beta)$, $c(\beta)^{\dagger}$ are related to c , c^{\dagger} via Eq. (11).

Inserting Eq. (A6) into Eq. (A1), the effective Hamiltonian becomes

$$\begin{aligned} \hat{H}(\beta) &= \varepsilon \left[\cos\beta \hat{J}_z(\beta) + \frac{1}{2} \sin\beta [\hat{J}_+(\beta) + \hat{J}_-(\beta)] \right] \\ &\quad - \frac{V}{4} [\sin^2\beta [4\hat{J}_z(\beta)^2 - \{\hat{J}_+(\beta), \hat{J}_-(\beta)\}] \\ &\quad + (1 + \cos^2\beta) [\hat{J}_+(\beta)^2 + \hat{J}_-(\beta)^2] \\ &\quad - 2\sin\beta \cos\beta \{\{\hat{J}_z(\beta), \hat{J}_+(\beta)\} + \{\hat{J}_z(\beta), \hat{J}_-(\beta)\}\}]. \end{aligned} \quad (\text{A10})$$

Matrix elements of the Hamiltonian between the many-body basis states $|n, \beta\rangle$ are determined by

$$\begin{aligned} \langle n', \beta | \hat{J}_z(\beta) | n, \beta \rangle &= M \delta_{n',n}, \\ \langle n', \beta | \hat{J}_\pm(\beta) | n, \beta \rangle &= \sqrt{J(J+1) - M(M\pm 1)} \delta_{n',n\pm 1}, \\ \langle n', \beta | \hat{J}_z(\beta)^2 | n, \beta \rangle &= M^2 \delta_{n',n}, \\ \langle n', \beta | \hat{J}_\pm(\beta)^2 | n, \beta \rangle &= \sqrt{J(J+1) - M(M\pm 1)} \sqrt{J(J+1) - (M\pm 2)(M\pm 1)} \delta_{n',n\pm 2}, \\ \langle n', \beta | \{\hat{J}_z(\beta), \hat{J}_\pm(\beta)\} | n, \beta \rangle &= (2M\pm 1) \sqrt{J(J+1) - M(M\pm 1)} \delta_{n',n\pm 1}, \\ \langle n', \beta | \{\hat{J}_+(\beta), \hat{J}_-(\beta)\} | n, \beta \rangle &= [2J(J+1) - 2M^2] \delta_{n',n}, \end{aligned} \quad (\text{A11})$$

where $J = N/2$ and $M = n - J = n - N/2$. This leads to

$$\begin{aligned} \langle n', \beta | \hat{H}(\beta) | n, \beta \rangle &= \left(\varepsilon \cos(\beta) \left(n - \frac{N}{2} \right) - \frac{V}{4} \sin^2(\beta) [N^2 + 6n^2 - 6nN - N] \right) \delta_{n',n} \\ &\quad + \frac{1}{2} \sqrt{(N-n)(n+1)} \sin(\beta) [\varepsilon - V \cos(\beta)(N - 2n - 1)] \delta_{n',n+1} \\ &\quad + \frac{1}{2} \sqrt{n(N-n+1)} \sin(\beta) [\varepsilon - V \cos(\beta)(N - 2n + 1)] \delta_{n',n-1} \\ &\quad - \frac{V}{4} (1 + \cos^2(\beta)) \sqrt{(N-n)(n+1)} \sqrt{(N-n-1)(n+2)} \delta_{n',n+2} \\ &\quad - \frac{V}{4} (1 + \cos^2(\beta)) \sqrt{(N-n+2)(n-1)} \sqrt{n(N-n+1)} \delta_{n',n-2}. \end{aligned} \quad (\text{A12})$$

When $\beta = 0$, the Hamiltonian in Eq. (A1), which does not connect configurations characterized by $n' = n \pm 1$, is recovered.

APPENDIX B: HAMILTONIAN LEARNING VARIATIONAL QUANTUM EIGENSOLVER (HL-VQE): MORE DETAILS

In this Appendix, we detail the hybrid algorithm that combines VQE with Hamiltonian learning to optimize the

efficacy of effective model spaces in recovering the lowest-lying states of the LMG model, as described in the main text. The Hamiltonian is uniquely defined with $\beta = 0$ in the full model space, and the lowest-lying states can be found by using, for example, the VQE algorithm with a quantum

computer, or variants thereof, if the system lies beyond the capabilities of classical computing. If available quantum resources are insufficient to accommodate the full Hamiltonian, then truncated systems can be implemented, but the Hamiltonian in the effective model space will include operators with coefficients that must be determined in addition to the parameters defining the ground state, or low-lying excited state wave functions. For a general system, we define the cost function for the variation to be the expectation value of the energy, which for the ground state is (with one variational parameter in the effective model space Hamiltonian)

$$E(\beta, \theta) = \langle \Psi(\theta) | \hat{H}(\beta) | \Psi(\theta) \rangle. \quad (\text{B1})$$

We assume that the functional dependence of $\hat{H}(\beta)$ on β can be determined classically, as is the case for the LMG model, and that the derivative $\frac{\partial}{\partial \beta} \hat{H}(\beta)$ can also be determined classically. While not required, it is further assumed that the Pauli decomposition of both can be readily determined classically. The usual arguments motivating the use of VQE to determine matrix elements of Pauli-operators in a quantum many-body wave function hold in this case, and therefore a quantum computer enables evaluation of parts of

$$E(\beta, \theta), \quad \frac{\partial}{\partial \beta} E(\beta, \theta), \quad \frac{\partial}{\partial \theta_i} E(\beta, \theta). \quad (\text{B2})$$

Using gradient descent to learn the parameters that minimize $E(\beta, \theta)$, and starting from initial values, $\beta^{[k=0]}$ and $\theta_i^{[k=0]}$, sets of evaluations are used to determine updated values for the next iteration,

$$\begin{aligned} \beta^{[k+1]} &= \beta^{[k]} - \eta \frac{\partial}{\partial \beta} E(\beta^{[k]}, \theta^{[k]}), \\ \theta_i^{[k+1]} &= \theta_i^{[k]} - \eta \frac{\partial}{\partial \theta_i} E(\beta^{[k]}, \theta^{[k]}), \end{aligned} \quad (\text{B3})$$

using a linear learning function, with a learning rate η iteratively tuned for optimal convergence. If the starting points for the parameters are within the domain of attraction of the optimal value, this system will iteratively converge to the optimal values. This simultaneous iteration and variation of parameters identifies the optimal variational ground-state wave function and learns the Hamiltonian in the effective model space by determining β . This method generalizes straightforwardly to multiple parameters defining an effective Hamiltonian.

1. One-qubit quantum circuits ($\Lambda = 2$ states)

An effective model space defined by one qubit is straightforward to study. The β -transformation described previously leads to an effective two-state Hamiltonian represented on one qubit that has a Pauli-decomposition,

$$\hat{H}^{(2)}(\beta) = h_x^{(2)}(\beta) \hat{X} + h_y^{(2)}(\beta) \hat{Y} + h_z^{(2)}(\beta) \hat{Z} + h_I^{(2)}(\beta) \hat{I}. \quad (\text{B4})$$

Defining the (real) wave function through a rotation about the y axis,

$$|\Psi(\theta)\rangle = \cos \frac{\theta}{2} |0\rangle + \sin \frac{\theta}{2} |1\rangle, \quad (\text{B5})$$

matrix elements of the Pauli operators are

$$\langle \hat{X} \rangle_\theta = \sin \theta, \quad \langle \hat{Y} \rangle_\theta = 0, \quad \langle \hat{Z} \rangle_\theta = \cos \theta, \quad \langle \hat{I}_2 \rangle_\theta = 1, \quad (\text{B6})$$

where $\langle \hat{O} \rangle_\theta \equiv \langle \Psi(\theta) | \hat{O} | \Psi(\theta) \rangle$. The computation of derivatives is straightforward using a finite-difference relation,

$$\begin{aligned} \frac{\partial}{\partial \theta} \langle \hat{X} \rangle_\theta &= \frac{1}{2} (\langle \hat{X} \rangle_{\theta+\pi/2} - \langle \hat{X} \rangle_{\theta-\pi/2}), \\ \frac{\partial}{\partial \theta} \langle \hat{Z} \rangle_\theta &= \frac{1}{2} (\langle \hat{Z} \rangle_{\theta+\pi/2} - \langle \hat{Z} \rangle_{\theta-\pi/2}), \end{aligned} \quad (\text{B7})$$

and is directly implementable on a quantum computer with two different ensemble measurements per operator. From these relations, the expectation value of the Hamiltonian is

$$\begin{aligned} \langle \hat{H}^{(2)}(\beta) \rangle_\theta &= h_I^{(2)}(\beta) + h_x^{(2)}(\beta) \langle \hat{X} \rangle_\theta + h_z^{(2)}(\beta) \langle \hat{Z} \rangle_\theta, \\ \frac{\partial}{\partial \beta} \langle \hat{H}^{(2)}(\beta) \rangle_\theta &= \frac{\partial}{\partial \beta} h_I^{(2)}(\beta) + \frac{\partial}{\partial \beta} h_x^{(2)}(\beta) \langle \hat{X} \rangle_\theta \\ &\quad + \frac{\partial}{\partial \beta} h_z^{(2)}(\beta) \langle \hat{Z} \rangle_\theta, \\ \frac{\partial}{\partial \theta} \langle \hat{H}^{(2)}(\beta) \rangle_\theta &= h_x^{(2)}(\beta) \frac{\partial}{\partial \theta} \langle \hat{X} \rangle_\theta + h_z^{(2)}(\beta) \frac{\partial}{\partial \theta} \langle \hat{Z} \rangle_\theta. \end{aligned} \quad (\text{B8})$$

A gradient-descent learning of β, θ involves iteratively applying

$$\begin{aligned} \beta^{[k+1]} &= \beta^{[k]} - \eta \frac{\partial}{\partial \beta} \langle \hat{H}^{(2)}(\beta^{[k]}) \rangle_{\theta^{[k]}}, \\ \theta^{[k+1]} &= \theta^{[k]} - \eta \frac{\partial}{\partial \theta} \langle \hat{H}^{(2)}(\beta^{[k]}) \rangle_{\theta^{[k]}}, \end{aligned} \quad (\text{B9})$$

until the parameters have reached stable values. The value of the learned parameters are found from the mean and standard deviation⁷ of the last n_{sel} parameters steps after the parameter sets have converged, where n_{sel} is typically taken to be $n_{\text{sel}} \gtrsim 10$, and determined by the quantum resources. The learning rate, η , is selected based upon the convergence behavior of the iteration. As is well known, a value that is too large leads to instability, and a value that is too small leads to large resource requirements.

Quantum circuits are used to prepare ensembles of states $|\Psi(\theta^{[k]})\rangle$, $|\Psi(\theta^{[k]} + \frac{\pi}{2})\rangle$, $|\Psi(\theta^{[k]} - \frac{\pi}{2})\rangle$, in which expectation values of \hat{X} and \hat{Z} are measured. The latter is in the computational basis and requires no further operations before measurement, while the former requires an application of a Hadamard gate. With classical computation of the $h_a^{(2)}(\beta^{[k]})$ and derivatives, this is sufficient to implement the learning in Eq. (B9), which will have efficacy dictated, in part, by the statistical and systematic errors associated with the quantum computations.

2. Two-qubit quantum Circuits ($\Lambda = 4$ states)

For an effective model space contained in two qubits, the protocol is analogous to that of one qubit, described above.

⁷Alternately, half of the difference between the maximum and minimum values in that interval could be quoted.

A real wave function on two qubits can be prepared by the quantum circuit shown in Fig. 12 in terms of three angles $\theta_{0,1,2}$. The $R_{ZX}(\theta)$ gate is available for the IBM's quantum computers, and we find it to be convenient for our purposes:

$$R_{ZX}(\theta) = e^{-i\theta\hat{X}\otimes\hat{Z}/2}. \quad (\text{B10})$$

The most general Hamiltonian for this system has the form, restricting ourselves again to one unknown parameter defining the Hamiltonian, β ,

$$H^{(4)}(\beta) = \sum_{i,j}^4 h_{ij}^{(4)}(\beta) \bar{\sigma}_i \bar{\sigma}_j, \quad (\text{B11})$$

where $\bar{\sigma} = \{\hat{X}, \hat{Y}, \hat{Z}, \hat{I}\}$. There are ten operator structures contributing to the Hamiltonian, with Pauli decomposition,

$$\begin{aligned} \langle H^{(4)}(\beta) \rangle_{\theta} &= h_{II}^{(4)}(\beta) + h_{xx}^{(4)}(\beta) \langle \hat{X} \otimes \hat{X} \rangle_{\theta} \\ &+ h_{xz}^{(4)}(\beta) \langle \hat{X} \otimes \hat{Z} \rangle_{\theta} + h_{xl}^{(4)}(\beta) \langle \hat{X} \otimes \hat{I} \rangle_{\theta} \\ &+ h_{yy}^{(4)}(\beta) \langle \hat{Y} \otimes \hat{Y} \rangle_{\theta} + h_{yx}^{(4)}(\beta) \langle \hat{Z} \otimes \hat{X} \rangle_{\theta} \\ &+ h_{zz}^{(4)}(\beta) \langle \hat{Z} \otimes \hat{Z} \rangle_{\theta} + h_{zl}^{(4)}(\beta) \langle \hat{Z} \otimes \hat{I} \rangle_{\theta} \\ &+ h_{Ix}^{(4)}(\beta) \langle \hat{I} \otimes \hat{X} \rangle_{\theta} + h_{Iz}^{(4)}(\beta) \langle \hat{I} \otimes \hat{Z} \rangle_{\theta}, \end{aligned} \quad (\text{B12})$$

with explicit expressions for the $h_{ab}^{(2)}(\beta)$ given in Eq. (31), and with expectation values in the wave function in Eq. (26),

$$\begin{aligned} \langle \hat{X} \otimes \hat{X} \rangle_{\theta} &= \sin \theta_0 \sin \theta_2, \\ \langle \hat{X} \otimes \hat{Z} \rangle_{\theta} &= \cos \theta_0 \cos \theta_1 \sin \theta_2 - \sin \theta_1 \cos \theta_2, \\ \langle \hat{X} \otimes \hat{I} \rangle_{\theta} &= \cos \theta_1 \sin \theta_2 - \cos \theta_0 \sin \theta_1 \cos \theta_2, \\ \langle \hat{Y} \otimes \hat{Y} \rangle_{\theta} &= -\sin \theta_0 \sin \theta_1, \\ \langle \hat{Z} \otimes \hat{X} \rangle_{\theta} &= \sin \theta_0 \cos \theta_2, \\ \langle \hat{Z} \otimes \hat{Z} \rangle_{\theta} &= \cos \theta_0 \cos \theta_1 \cos \theta_2 + \sin \theta_1 \sin \theta_2, \\ \langle \hat{Z} \otimes \hat{I} \rangle_{\theta} &= \cos \theta_0 \sin \theta_1 \sin \theta_2 + \cos \theta_1 \cos \theta_2, \\ \langle \hat{I} \otimes \hat{X} \rangle_{\theta} &= \sin \theta_0 \cos \theta_1, \\ \langle \hat{I} \otimes \hat{Z} \rangle_{\theta} &= \cos \theta_0, \\ \langle \hat{I} \otimes \hat{I} \rangle_{\theta} &= 1. \end{aligned} \quad (\text{B13})$$

Derivatives of $\langle H^{(4)}(\beta) \rangle_{\theta}$ with respect to the θ_i ($i = 0, 1, 2$) can be found from finite differences, analogous to the single qubit case, e.g.,

$$\begin{aligned} &\frac{\partial}{\partial \theta_0} \langle \hat{X} \otimes \hat{X} \rangle_{\theta} \\ &= \frac{1}{2} (\langle \hat{X} \otimes \hat{X} \rangle_{(\theta_0+\frac{\pi}{2}, \theta_1, \theta_2)} - \langle \hat{X} \otimes \hat{X} \rangle_{(\theta_0-\frac{\pi}{2}, \theta_1, \theta_2)}). \end{aligned} \quad (\text{B14})$$

This relation can be used for all of the operators for $\theta_{0,1,2}$, made possible by the structure of the quantum circuit in Fig. 12, where each angle only appears in one gate in the operator.

In our quantum simulations, for a given set of θ_i , the circuit in Fig. 12 prepares the wave function on the two qubits. This is performed for seven quantum circuits, with parameters $(\theta_0, \theta_1, \theta_2)$, $(\theta_0 \pm \pi/2, \theta_1, \theta_2)$, $(\theta_0, \theta_1 \pm \pi/2, \theta_2)$, and $(\theta_0, \theta_1, \theta_2 \pm \pi/2)$. Matrix elements of the operators $\hat{Z} \otimes \hat{Z}$, $\hat{I} \otimes \hat{Z}$, and $\hat{Z} \otimes \hat{I}$ can be constructed from combinations of measurements of the circuit in the computational basis. Matrix elements of operators $\hat{X} \otimes \hat{X}$, $\hat{I} \otimes \hat{X}$, $\hat{X} \otimes \hat{I}$, $\hat{Z} \otimes \hat{X}$, and $\hat{X} \otimes \hat{Z}$ can be found by adding a Hadamard gate, \hat{H} , to the qubits with \hat{X} operators, and then performing measurements in the computational basis. For $\hat{Y} \otimes \hat{Y}$, adding \hat{S}^{\dagger} followed by \hat{H} to both qubits rotates the system into the computational basis. If $\{p_{00}, p_{11}, p_{01}, p_{10}\}$ are the probabilities of outcomes in the computational basis, then contracting with the vectors $\{1, 1, -1, -1\}$ gives the matrix element of $\hat{X} \otimes \hat{X}$ or $\hat{Y} \otimes \hat{Y}$ or $\hat{Z} \otimes \hat{Z}$ or $\hat{X} \otimes \hat{Z}$ or $\hat{Z} \otimes \hat{X}$, $\{1, -1, -1, 1\}$ gives the matrix element of $\hat{Z} \otimes \hat{I}$ or $\hat{X} \otimes \hat{I}$, and $\{1, -1, 1, -1\}$ gives the matrix element of $\hat{I} \otimes \hat{Z}$ or $\hat{I} \otimes \hat{X}$.

The gradient descent takes a form analogous to that for one qubit, iterating on β and $\theta_{0,1,2}$:

$$\begin{aligned} \beta^{[k+1]} &= \beta^{[k]} - \eta \frac{\partial}{\partial \beta} \langle \hat{H}^{(4)}(\beta^{[k]}) \rangle_{\theta^{[k]}}, \\ \theta_0^{[k+1]} &= \theta_0^{[k]} - \eta \frac{\partial}{\partial \theta_0} \langle \hat{H}^{(4)}(\beta^{[k]}) \rangle_{\theta^{[k]}}, \\ \theta_1^{[k+1]} &= \theta_1^{[k]} - \eta \frac{\partial}{\partial \theta_1} \langle \hat{H}^{(4)}(\beta^{[k]}) \rangle_{\theta^{[k]}}, \\ \theta_2^{[k+1]} &= \theta_2^{[k]} - \eta \frac{\partial}{\partial \theta_2} \langle \hat{H}^{(4)}(\beta^{[k]}) \rangle_{\theta^{[k]}}. \end{aligned} \quad (\text{B15})$$

APPENDIX C: GROUND STATES IN THE EFFECTIVE MODEL SPACES

The ground states of the LMG model in the effective model spaces have a particular form for the parameters that we have chosen to work with. In particular, the highest-lying odd p-h configuration has a vanishing amplitude independent of the size of the space.

1. Vanishing of the 1p-1h amplitude for $\Lambda = 2$

For the effective model space defined on a single qubit, and for the parameters we are working with, the Hamiltonian in Eq. (29) can be written as, for $\bar{v} = (N-1)V/\varepsilon > 0$,

$$\begin{aligned} H^{(2)}(\beta) &= \begin{pmatrix} h_{11}^{(2)} & h_{12}^{(2)} \\ h_{12}^{(2)} & h_{22}^{(2)} \end{pmatrix}, \\ h_{11}^{(2)} &= -\frac{1}{4}N\varepsilon[2\cos(\beta) + |\bar{v}|\sin^2(\beta)], \\ h_{12}^{(2)} &= -\frac{1}{2}\sqrt{N}\varepsilon\sin(\beta)[|\bar{v}|\cos(\beta) - 1], \\ h_{22}^{(2)} &= h_{11}^{(1)} + \varepsilon(\cos(\beta) + \frac{3}{2}|\bar{v}|\sin^2(\beta)), \end{aligned} \quad (\text{C1})$$

from which we see that $h_{11}^{(2)}, h_{22}^{(2)} \sim N$ and $h_{12}^{(2)} \sim \sqrt{N}$ and $h_{11}^{(2)} - h_{22}^{(2)} \sim 1$. The minimum eigenvalue of this system is

obtained at a value of β such that $h_{12}^{(2)} = 0$. This is not so obvious from the matrix itself, but can be found from a stability argument around this condition. Writing $\beta = \cos^{-1}(\frac{1}{|\bar{v}|}) + \delta_\beta$, the eigenvalues are found to be

$$E_{\text{g.s.}} = -\frac{N(|\bar{v}|^2 + 1)\varepsilon}{4|\bar{v}|} + \delta_\beta^2 \frac{N|\bar{v}|(|\bar{v}|^2 + 1)\varepsilon}{4(3|\bar{v}|^2 - 1)},$$

$$E_1 = E_{\text{g.s.}} + \frac{(3|\bar{v}|^2 - 1)\varepsilon}{2|\bar{v}|} - 2\varepsilon\delta_\beta. \quad (\text{C2})$$

From these expressions, it is clear that for $\delta_\beta \sim 1/\sqrt{N}$ the eigenvalues do not invert and the extremum occurs at $\delta_\beta = 0$. Consequently, the eigenvector at the minimum is entirely 0p-0h configuration, corresponding to the HF wave function. Numerically, this is found to be true for the explored parameter space even for small N .

2. Vanishing of the 3p-3h amplitude for $\Lambda = 4$

The structure of the Hamiltonian, particularly the degree of symmetry that renders the LMG-model solvable, leads to ground states with some properties that are naively unexpected. One of those properties is the vanishing of the 3p-3h amplitude in the four-state effective model space, and generally the vanishing of the $(\Lambda - 1)p - (\Lambda - 1)h$ amplitude in the Λ model space. The origin of this can be seen by considering the N scaling of the elements of the Hamiltonian,

$$H^{(4)}(\beta) \sim \begin{pmatrix} N & \sqrt{N} & 1 & 0 \\ \sqrt{N} & N & \sqrt{N} & 1 \\ 1 & \sqrt{N} & N & \sqrt{N} \\ 0 & 1 & \sqrt{N} & N \end{pmatrix}, \quad (\text{C3})$$

where the entries denote the maximum power of N . The scaling of the diagonal entries remains the same after subtracting the identity contribution. We diagonalize the upper-left 3×3 block of this matrix with a transformation S ,

$$S = \left(\begin{array}{c|c} \mathbf{U} & \mathbf{0} \\ \hline \mathbf{0} & 1 \end{array} \right),$$

$$\bar{H}^{(4)}(\beta) = S \cdot H^{(4)}(\beta) \cdot S^\dagger = \left(\begin{array}{c|c} H_{3,\text{diag}}^{(4)}(\beta) & \Gamma \\ \hline \Gamma^\dagger & \delta \end{array} \right), \quad (\text{C4})$$

where $H_{3,\text{diag}}^{(4)}(\beta)$ is a diagonal 3×3 matrix and $\delta \sim N$. Because of the hierarchy explicit in Eq. (C3), the transformation \mathbf{U} is of the form $\mathbf{U} \sim I_3 + \xi^a T^a$, where $\xi^a \sim 1/\sqrt{N}$ and T^a are the generators of $SU(3)$. Thus, the elements of Γ scale at most as $\Gamma \sim \sqrt{N}$, and the element of Γ corresponding to

the lowest eigenvalue, $E_{\text{g.s.},3}$ scales attached most as $\Gamma_1 \sim 1$ (compared to the diagonal element that scales as $\sim N$). Returning to diagonalizing $\bar{H}^{(4)}(\beta)$, by considering perturbations in $1/N$, the lowest eigenvalue corresponding to an eigenvector of the form $\mathbf{d}^{(2)} = (1, 0, 0, \alpha)^T / \sqrt{1 + |\alpha|^2}$ is of the form

$$E_{\text{g.s.}}^{(4)} = \frac{1}{1 + |\alpha|^2} [E_{\text{g.s.},3} + |\alpha|^2 \Gamma_1]. \quad (\text{C5})$$

For $\Gamma_1 > E_{\text{g.s.},3}$, which is manifest from the N scaling, the minimum energy is obtained for $\alpha = 0$, corresponding to $E_{\text{g.s.}}^{(4)} = E_{\text{g.s.},3}$.

If we had assumed from the start that the amplitude of the 3p-3h configuration vanished, only two parameters would have been required to parametrize the wave function. From the previous subsection, enforcing the vanishing of the 3p-3h configuration requires $\theta_1 + \theta_2 = 0$. As such, a more compact circuit could have been used with just two independent angles defining the wave function, or the circuit in Fig. 12 can be used, with a modified gradient descent.

APPENDIX D: COMMENTS ON THE METHODS USED IN THE QUANTUM SIMULATIONS USING IBM'S QUANTUM COMPUTERS

Standard techniques and QISKIT [58] packages were used to produce results from IBM's QExperience [53] AER and `ibm_lagos`. PYTHON [102] and JUPYTER notebooks [103] were used as an interface after developing codes with *Mathematica* [104]. The Hamiltonian coefficients and derivatives were included as function calls, as were the state-preparation quantum circuits. Measurement errors were mitigated using the standard packages in QISKIT [58], `TensoredMeasFitter` and `meas_fitter`, but the errors associated with entangling operations and decoherence were not mitigated as the implemented circuits are sufficiently shallow. A higher precision simulation would require such mitigation. The quantum circuits were transpiled onto the qubits with the highest fidelity (as determined from the most recent calibration) consistent with not using swap gates, for example, `qc2t = transpile(qc2a, backend=backend, optimization_level=3)`. When multiple circuits were executed, the measurements related to one of the circuits were determined by tracing over the other qubits.

The workflow was implemented with an initialization of the IBMQ environment, functions and subroutines. Gradient descent was accomplished with a `for` loop that generated the quantum circuits, submitted them to the device queue, postprocessed the results to determine the energy, amplitudes and gradients, appended them to appropriate arrays, determined updated values of the variational parameters, and then repeated until the iteration limit was exceeded.

The following codesnippets were used to determine the matrix elements of, as an example, $\hat{X}\hat{X}$ from the variational wave function in the two-qubit simulations:

```

# XX
qc0 = QuantumCircuit(nQ, nQ)
qc0 = iniwaveRZX(qc0, theta0, theta1, theta2, cq0, cq1)
qc0.h(cq0)
qc0.h(cq1)
qc0.measure([0,1,2,3], [0,1,2,3])
for ntnt in range(nTwirl):
qc0a = qc0
qc0t = transpile(qc0a, backend=backend, optimization_level=3)
circ_list.append(qc0t)
.
.
.
qc3 = QuantumCircuit(nQ, nQ)
qc3 = iniwaveRZX(qc3, theta0, theta1, theta2+npihalf, cq0, cq1)
qc3 = iniwaveRZX(qc3, theta0, theta1, theta2-npihalf, cq2, cq3)
qc3.h(cq0)
qc3.h(cq1)
qc3.h(cq2)
qc3.h(cq3)
qc3.measure([0,1,2,3], [0,1,2,3])
for ntnt in range(nTwirl):
qc3a = qc3
qc3t = transpile(qc3a, backend=backend, optimization_level=3)
circ_list.append(qc3t)
using the function
def iniwaveRZX(qc, ttt0, ttt1, ttt2, s0, s1):
qc.ry(ttt0, s1)
qc.s(s0)
qc.rzx(ttt1, s1, s0)
qc.sdg(s0)
qc.ry(ttt2, s0)
return qc

```

corresponding to Fig. 12.

APPENDIX E: EXCITED STATES

Finding the excited states in the effective model space is straightforward using chemical potentials, as demonstrated in Ref. [105]. A chemical potential can be given to the ground-state wave function of sufficient size to move the state high into the spectrum, above the first excited state, and the ground state of this new system is the first excited state. Adding a chemical potential μ_0 to Eq. (24) for the ground state $|\Psi\rangle^{(\Lambda)}$,

$$\hat{H}'(\beta_0) = \hat{H}(\beta_0) + \mu_0 |\Psi\rangle^{(\Lambda)(\Lambda)} \langle \Psi|, \quad (E1)$$

where $\beta = \beta_0$ is the value optimized for the ground state, furnishes a Hamiltonian which can be used with the VQE algorithm (or others) to variationally find the first excited state. Tracing against products of Pauli matrices, $\bar{\sigma}_{i_1} \otimes \dots \otimes \bar{\sigma}_{i_M}$, allows this modified Hamiltonian to be written as

$$\hat{H}'(\beta_0) = \sum_{i_1, \dots, i_M=1}^4 h'_{i_1, \dots, i_M}(\beta_0) \bar{\sigma}_{i_1} \otimes \dots \otimes \bar{\sigma}_{i_M},$$

$$h' = h + \frac{\mu_0}{2^M} \langle \Psi | \bar{\sigma}_{i_1} \otimes \dots \otimes \bar{\sigma}_{i_M} | \Psi \rangle^{(\Lambda)}, \quad (E2)$$

which can be evaluated straightforwardly as the matrix elements of the Pauli operators in the ground state have already been determined. The ground state of $\hat{H}'(\beta_0)$ can be determined using VQE, thereby providing the energy and wave function of the first excited state in the effective model space. Higher excited states can be determined by repeated application of this procedure. As shown in Refs. [105] and [92], the repeated application can lead to an accumulation of errors in the effective Hamiltonian for highly excited states.

We note that the procedure described above means that the same effective Hamiltonian determines the ground and excited states, which are orthonormal. In principle, the Hamiltonian parameter could be optimized for each state, which would lead to nonorthogonal states, but would provide a better approximation to the exact states. From an EFT perspective, this corresponds to resumming contributions from an infinite number of higher-order operators differently for each state (with the difference vanishing for increasing size of model space). It then becomes interesting to understand better the form of perturbation theory that could be used to systematically include residual (higher-order) terms in the Hamiltonian.

One can potentially force the orthogonality of the ground and excited states via the addition of constraints [106]. Another approach, which appears to be widely used in quantum chemistry, is to determine the orbitals via state-averaged variational calculations [107,108], so that the resulting single-particle basis contains information about both ground and excited states correlations. The latter technique provides some sort of compromise as the orthonormality of the states is automatically fulfilled, at the price of potentially degrading the quality of each individual state.

APPENDIX F: TABLES OF THE RESULTS SHOWN IN THE FIGURES

Tables V–XII present the numerical results shown in Figs. 13–17.

TABLE V. Central values of one-qubit quantum simulations obtained using AER simulator for the ground-state energy (in units of ε), wave function amplitudes, and Bures distances [Eq. (19)] for the $\Lambda = 2$ effective model space using 100 k shots per ensemble. The LMG model parameters are $N = 30$, $\varepsilon = 1.0$, $\bar{v} = 2.0$. The starting values of variational parameters were $\beta^{[0]} = 0.2$ and $\theta_i^{[0]} = 0.30$.

$\Lambda = 2$, AER				
Iteration	Energy	$ A_0 $	$ A_1 $	Bures distance
1	-15.43	0.9879	0.1550	1.229
2	-15.66	0.9869	0.1613	1.179
3	-15.94	0.9858	0.1678	1.119
4	-16.24	0.9846	0.1746	1.048
5	-16.56	0.9834	0.1814	0.9676
6	-16.91	0.9821	0.1882	0.8762
7	-17.24	0.9808	0.1949	0.7749
8	-17.57	0.9795	0.2014	0.6649
9	-17.89	0.9783	0.2074	0.5487
10	-18.15	0.9771	0.2128	0.4307
11	-18.37	0.9761	0.2172	0.3200
12	-18.55	0.9757	0.2191	0.2390
13	-18.66	0.9769	0.2138	0.2249
14	-18.69	0.9805	0.1965	0.2162
15	-18.70	0.9831	0.1829	0.2143
16	-18.71	0.9856	0.1691	0.2104
17	-18.71	0.9876	0.1573	0.2084
18	-18.72	0.9893	0.1458	0.2059
19	-18.72	0.9908	0.1353	0.2041
20	-18.73	0.9921	0.1252	0.2017
21	-18.73	0.9932	0.1165	0.2010
22	-18.73	0.9942	0.1078	0.1997
23	-18.73	0.9950	0.09995	0.1984
24	-18.74	0.9956	0.09333	0.1975
25	-18.74	0.9962	0.08662	0.1973
26	-18.74	0.9968	0.07996	0.1958
27	-18.74	0.9972	0.07458	0.1953
28	-18.74	0.9976	0.06978	0.1954

TABLE V. (Continued.)

$\Lambda = 2$, AER				
Iteration	Energy	$ A_0 $	$ A_1 $	Bures distance
29	-18.74	0.9979	0.06461	0.1954
30	-18.74	0.9982	0.05996	0.1946
31	-18.75	0.9985	0.05552	0.1939
32	-18.75	0.9986	0.05197	0.1938
33	-18.75	0.9988	0.04821	0.1933
34	-18.75	0.9990	0.04518	0.1940
35	-18.75	0.9991	0.04158	0.1934
36	-18.75	0.9993	0.03870	0.1932
37	-18.75	0.9993	0.03634	0.1931
38	-18.75	0.9994	0.03370	0.1939
39	-18.75	0.9995	0.03104	0.1927
40	-18.75	0.9996	0.02922	0.1931
41	-18.75	0.9996	0.02728	0.1928
42	-18.75	0.9997	0.02535	0.1926
43	-18.75	0.9997	0.02321	0.1927
44	-18.75	0.9998	0.02172	0.1925
45	-18.75	0.9998	0.02003	0.1925
46	-18.75	0.9998	0.01867	0.1930
47	-18.75	0.9999	0.01708	0.1921
48	-18.75	0.9999	0.01595	0.1926
49	-18.75	0.9999	0.01493	0.1925
50	-18.75	0.9999	0.01389	0.1925
51	-18.75	0.9999	0.01264	0.1928
52	-18.75	0.9999	0.01129	0.1927
53	-18.75	0.9999	0.01003	0.1922
54	-18.75	1.000	0.009508	0.1926
55	-18.75	1.000	0.008560	0.1921
56	-18.75	1.000	0.007880	0.1928
57	-18.75	1.000	0.007372	0.1921
58	-18.75	1.000	0.007416	0.1925
59	-18.75	1.000	0.006891	0.1921
60	-18.75	1.000	0.006850	0.1930
61	-18.75	1.000	0.006336	0.1921
62	-18.75	1.000	0.006331	0.1927
63	-18.75	1.000	0.005625	0.1927
64	-18.75	1.000	0.005190	0.1927
65	-18.75	1.000	0.005027	0.1919
66	-18.75	1.000	0.005102	0.1926
67	-18.75	1.000	0.004761	0.1928
68	-18.75	1.000	0.004395	0.1928
69	-18.75	1.000	0.003703	0.1922
70	-18.75	1.000	0.003271	0.1927
71	-18.75	1.000	0.002348	0.1918
72	-18.75	1.000	0.002814	0.1932
73	-18.75	1.000	0.002179	0.1924
74	-18.75	1.000	0.001911	0.1928
75	-18.75	1.000	0.001652	0.1926
76	-18.75	1.000	0.001393	0.1926
77	-18.75	1.000	0.001261	0.1925
78	-18.75	1.000	0.001172	0.1925
79	-18.75	1.000	0.0008452	0.1923
80	-18.75	1.000	0.001096	0.1929

TABLE VI. Central values of one-qubit quantum simulations obtained using `ibm_lagos` for the ground-state energy (in units of ε), wave function amplitudes, and Bures distances [Eq. (19)] for the $\Lambda = 2$ effective model space using 32 k shots per ensemble. The LMG model parameters are $N = 30$, $\varepsilon = 1.0$, $\bar{v} = 2.0$. The starting values of variational parameters were $\beta^{(0)} = 0.2$ and $\theta_i^{(0)} = 0.10$.

$\Lambda = 2, \text{ibm_lagos}$				
Iteration	Energy	$ A_0 $	$ A_1 $	Bures distance
1	-15.33	0.9982	0.06027	1.243
2	-15.60	0.9975	0.07069	1.186
3	-15.91	0.9967	0.08118	1.116
4	-16.25	0.9958	0.09165	1.032
5	-16.65	0.9948	0.1018	0.9335
6	-17.06	0.9937	0.1120	0.8204
7	-17.49	0.9925	0.1220	0.6944
8	-17.81	0.9913	0.1314	0.5583
9	-18.16	0.9901	0.1403	0.4179
10	-18.46	0.9890	0.1482	0.2873
11	-18.66	0.9881	0.1537	0.2083
12	-18.72	0.9891	0.1471	0.2140
13	-18.72	0.9914	0.1310	0.2011
14	-18.71	0.9924	0.1228	0.2052
15	-18.72	0.9938	0.1110	0.1986
16	-18.73	0.9946	0.1034	0.2017
17	-18.73	0.9956	0.09329	0.1971
18	-18.74	0.9963	0.08597	0.1970
19	-18.73	0.9969	0.07820	0.1961
20	-18.75	0.9974	0.07203	0.1949
21	-18.74	0.9978	0.06672	0.1951
22	-18.74	0.9981	0.06094	0.1945
23	-18.74	0.9984	0.05637	0.1949
24	-18.76	0.9987	0.05183	0.1922
25	-18.76	0.9988	0.04881	0.1923
26	-18.75	0.9989	0.04652	0.1952
27	-18.74	0.9991	0.04197	0.1935
28	-18.75	0.9992	0.03876	0.1933
29	-18.74	0.9994	0.03522	0.1922
30	-18.74	0.9995	0.03311	0.1946
31	-18.75	0.9996	0.02958	0.1922
32	-18.75	0.9996	0.02833	0.1916
33	-18.75	0.9996	0.02764	0.1955
34	-18.75	0.9997	0.02354	0.1906
35	-18.75	0.9997	0.02406	0.1903
36	-18.75	0.9997	0.02501	0.1938
37	-18.75	0.9998	0.02224	0.1907
38	-18.75	0.9997	0.02339	0.1981

TABLE VI. (Continued.)

$\Lambda = 2, \text{ibm_lagos}$				
Iteration	Energy	$ A_0 $	$ A_1 $	Bures distance
39	-18.75	0.9998	0.01918	0.1923
40	-18.74	0.9998	0.01891	0.1948
41	-18.75	0.9999	0.01641	0.1922
42	-18.75	0.9999	0.01604	0.1923
43	-18.75	0.9999	0.01448	0.1926
44	-18.75	0.9999	0.01274	0.1901
45	-18.75	0.9999	0.01409	0.1934
46	-18.75	0.9999	0.01251	0.1900
47	-18.75	0.9999	0.01391	0.1954
48	-18.75	0.9999	0.01204	0.1926
49	-18.75	0.9999	0.01266	0.1935
50	-18.75	0.9999	0.01233	0.1898
51	-18.75	0.9999	0.01492	0.1902
52	-18.75	0.9999	0.01574	0.1921
53	-18.75	0.9999	0.01413	0.1922
54	-18.74	0.9999	0.01312	0.1924
55	-18.75	0.9999	0.01175	0.1924
56	-18.75	0.9999	0.01091	0.1923
57	-18.74	1.000	0.009768	0.1924
58	-18.75	1.000	0.009526	0.1921
59	-18.74	1.000	0.008957	0.1938
60	-18.74	1.000	0.007376	0.1913
61	-18.75	1.000	0.008537	0.1931
62	-18.74	1.000	0.007399	0.1922
63	-18.75	1.000	0.006512	0.1915
64	-18.75	1.000	0.006302	0.1910
65	-18.75	1.000	0.006617	0.1925
66	-18.75	1.000	0.005911	0.1919
67	-18.73	1.000	0.005819	0.1925
68	-18.72	1.000	0.005404	0.1929
69	-18.75	1.000	0.005169	0.1920
70	-18.75	1.000	0.004952	0.1914
71	-18.75	1.000	0.004762	0.1923
72	-18.75	1.000	0.004237	0.1916
73	-18.74	1.000	0.004602	0.1937
74	-18.75	1.000	0.003239	0.1912
75	-18.74	1.000	0.003477	0.1928
76	-18.74	1.000	0.002555	0.1923
77	-18.74	1.000	0.002776	0.1931
78	-18.74	1.000	0.001708	0.1908
79	-18.75	1.000	0.003603	0.1934
80	-18.75	1.000	0.002328	0.1923

TABLE VII. Central values of 2-qubit quantum simulations obtained using AER simulator for the ground-state energy (in units of ε), wave function amplitudes, and Bures distances [Eq. (19)] for the $\Lambda = 4$ effective model space using 100 k shots per ensemble. The LMG model parameters are $N = 30$, $\varepsilon = 1.0$, $\bar{v} = 2.0$. The starting values of variational parameters were $\beta^{[0]} = 0.2$ and $\theta_i^{[0]} = 0.0$.

$\Lambda = 4$, AER						
Iteration	Energy	$ A_0 $	$ A_1 $	$ A_2 $	$ A_3 $	Bures distance
1	-17.98	0.9957	0.05494	-0.07397	1.933×10^{-6}	0.4320
2	-18.32	0.9972	0.05962	-0.04422	7.771×10^{-6}	0.2953
3	-18.57	0.9980	0.06343	-0.006676	0.00001920	0.2031
4	-18.72	0.9969	0.06415	0.04478	0.00004183	0.1606
5	-18.81	0.9935	0.05956	0.09709	0.00004846	0.1048
6	-18.87	0.9900	0.05837	0.1283	0.00006483	0.08426
7	-18.89	0.9879	0.05568	0.1449	0.00007499	0.06657
8	-18.90	0.9862	0.05564	0.1557	0.00008579	0.06405
9	-18.90	0.9855	0.05388	0.1607	0.00008767	0.05761
10	-18.90	0.9849	0.05401	0.1645	0.00009111	0.05843
11	-18.90	0.9847	0.05283	0.1658	0.00009575	0.05548
12	-18.90	0.9845	0.05294	0.1672	0.0001050	0.05667
13	-18.90	0.9845	0.05202	0.1675	0.0001009	0.05489
14	-18.90	0.9844	0.05202	0.1680	0.0001081	0.05598
15	-18.90	0.9845	0.05128	0.1678	0.0001130	0.05491
16	-18.90	0.9844	0.05118	0.1682	0.0001217	0.05545
17	-18.90	0.9845	0.05062	0.1681	0.0001216	0.05497
18	-18.90	0.9844	0.05053	0.1683	0.0001279	0.05529
19	-18.90	0.9845	0.05015	0.1681	0.0001343	0.05515
20	-18.90	0.9845	0.04993	0.1682	0.0001389	0.05536
21	-18.90	0.9845	0.04951	0.1681	0.0001400	0.05504
22	-18.90	0.9845	0.04935	0.1682	0.0001538	0.05530
23	-18.90	0.9846	0.04893	0.1680	0.0001561	0.05512
24	-18.90	0.9846	0.04878	0.1681	0.0001551	0.05535
25	-18.90	0.9846	0.04847	0.1680	0.0001555	0.05501
26	-18.90	0.9846	0.04836	0.1681	0.0001546	0.05535
27	-18.90	0.9846	0.04810	0.1681	0.0001561	0.05524
28	-18.90	0.9846	0.04785	0.1681	0.0001623	0.05517
29	-18.90	0.9846	0.04764	0.1680	0.0001607	0.05515
30	-18.90	0.9846	0.04751	0.1681	0.0001686	0.05526
31	-18.90	0.9847	0.04735	0.1679	0.0001703	0.05531
32	-18.90	0.9847	0.04711	0.1680	0.0001756	0.05538
33	-18.90	0.9847	0.04687	0.1679	0.0001738	0.05518
34	-18.90	0.9847	0.04668	0.1679	0.0001804	0.05553
35	-18.90	0.9847	0.04637	0.1678	0.0001792	0.05518
36	-18.90	0.9847	0.04635	0.1679	0.0001825	0.05551
37	-18.90	0.9848	0.04608	0.1678	0.0001847	0.05525
38	-18.90	0.9847	0.04592	0.1678	0.0001865	0.05548
39	-18.90	0.9848	0.04575	0.1677	0.0001945	0.05528
40	-18.90	0.9848	0.04561	0.1677	0.0002003	0.05574
41	-18.90	0.9848	0.04527	0.1676	0.0001977	0.05524
42	-18.90	0.9848	0.04521	0.1678	0.0001995	0.05558
43	-18.90	0.9848	0.04501	0.1676	0.0002030	0.05538
44	-18.90	0.9848	0.04480	0.1676	0.0002015	0.05558
45	-18.90	0.9849	0.04461	0.1675	0.0001946	0.05550
46	-18.90	0.9848	0.04447	0.1677	0.0001984	0.05537
47	-18.90	0.9848	0.04437	0.1677	0.0002005	0.05539
48	-18.90	0.9849	0.04425	0.1677	0.0001999	0.05553
49	-18.90	0.9849	0.04412	0.1677	0.0001998	0.05540
50	-18.90	0.9849	0.04406	0.1676	0.0001998	0.05561
51	-18.90	0.9849	0.04388	0.1674	0.0001987	0.05559
52	-18.90	0.9849	0.04372	0.1675	0.0001946	0.05546

TABLE VII. (Continued.)

$\Lambda = 4$, AER						
Iteration	Energy	$ A_0 $	$ A_1 $	$ A_2 $	$ A_3 $	Bures distance
53	-18.90	0.9849	0.04361	0.1675	0.0001972	0.05569
54	-18.90	0.9849	0.04345	0.1675	0.0001945	0.05544
55	-18.90	0.9849	0.04345	0.1676	0.0001951	0.05558
56	-18.90	0.9849	0.04338	0.1676	0.0001980	0.05552
57	-18.90	0.9849	0.04328	0.1676	0.0002018	0.05555
58	-18.90	0.9849	0.04319	0.1675	0.0002033	0.05551
59	-18.90	0.9849	0.04311	0.1674	0.0002049	0.05579
60	-18.90	0.9850	0.04290	0.1673	0.0002034	0.05547
61	-18.90	0.9849	0.04286	0.1675	0.0002040	0.05571
62	-18.90	0.9850	0.04267	0.1674	0.0002031	0.05540
63	-18.90	0.9850	0.04274	0.1674	0.0002060	0.05598
64	-18.90	0.9850	0.04253	0.1673	0.0002066	0.05547
65	-18.90	0.9850	0.04253	0.1675	0.0002075	0.05564
66	-18.90	0.9850	0.04244	0.1674	0.0002078	0.05553
67	-18.90	0.9850	0.04241	0.1675	0.0002079	0.05578
68	-18.90	0.9850	0.04223	0.1675	0.0002052	0.05553
69	-18.90	0.9850	0.04225	0.1675	0.0002076	0.05558
70	-18.90	0.9850	0.04221	0.1675	0.0002079	0.05548
71	-18.90	0.9850	0.04218	0.1675	0.0002032	0.05561
72	-18.90	0.9850	0.04211	0.1675	0.0002007	0.05561
73	-18.90	0.9850	0.04205	0.1673	0.0001984	0.05560
74	-18.90	0.9850	0.04202	0.1673	0.0002026	0.05565
75	-18.90	0.9850	0.04196	0.1674	0.0002035	0.05553
76	-18.90	0.9850	0.04191	0.1674	0.0002033	0.05559
77	-18.90	0.9850	0.04180	0.1674	0.0002079	0.05553
78	-18.90	0.9850	0.04183	0.1673	0.0002082	0.05565
79	-18.90	0.9850	0.04173	0.1674	0.0002081	0.05555
80	-18.90	0.9850	0.04171	0.1674	0.0002119	0.05571

TABLE VIII. Central values of 2-qubit quantum simulations obtained using `ibm_lagos` for the ground-state energy (in units of ε), wave function amplitudes, and Bures distances [Eq. (19)] for the $\Lambda = 4$ effective model space using 32k shots per ensemble. The LMG model parameters are $N = 30$, $\varepsilon = 1.0$, $\bar{v} = 2.0$. The starting values of variational parameters were $\beta^{[0]} = 0.2$ and $\theta_i^{[0]} = 0.0$.

$\Lambda = 4$, <code>ibm_lagos</code>						
Iteration	Energy	$ A_0 $	$ A_1 $	$ A_2 $	$ A_3 $	Bures distance
1	-15.32	0.9999	0.006064	0.01473	3.807×10^{-6}	1.256
2	-15.55	0.9996	0.01218	0.02589	0.00001039	1.203
3	-15.90	0.9992	0.01849	0.03509	0.00001715	1.138
4	-16.24	0.9987	0.02476	0.04357	0.00001987	1.061
5	-16.54	0.9982	0.03083	0.05049	0.00002447	0.9690
6	-16.96	0.9977	0.03698	0.05680	0.00003040	0.8638
7	-17.35	0.9971	0.04354	0.06307	0.00003385	0.7457
8	-17.76	0.9963	0.05009	0.06948	0.00005767	0.6161
9	-18.05	0.9956	0.05601	0.07560	0.00009977	0.4770
10	-18.42	0.9947	0.06213	0.08194	0.0001186	0.3326
11	-18.63	0.9938	0.06759	0.08814	0.0001753	0.1916
12	-18.79	0.9925	0.07196	0.09833	0.0002948	0.1013
13	-18.89	0.9914	0.07163	0.1097	0.0003181	0.09405
14	-18.87	0.9907	0.07054	0.1160	0.0003484	0.09040
15	-18.91	0.9902	0.06760	0.1219	0.0004992	0.08092
16	-18.86	0.9894	0.06633	0.1290	0.0006422	0.07533

TABLE VIII. (*Continued.*)

$\Lambda = 4, \text{ibm_lagos}$						
Iteration	Energy	$ A_0 $	$ A_1 $	$ A_2 $	$ A_3 $	Bures distance
17	-18.88	0.9888	0.06595	0.1342	0.0006689	0.07526
18	-18.88	0.9887	0.06438	0.1353	0.0007022	0.07114
19	-18.90	0.9878	0.06406	0.1418	0.0007734	0.06634
20	-18.90	0.9871	0.06346	0.1471	0.0007934	0.06667
21	-18.89	0.9875	0.06104	0.1456	0.0007279	0.06377
22	-18.88	0.9874	0.06016	0.1461	0.0007626	0.06292
23	-18.88	0.9871	0.06019	0.1485	0.0009840	0.06102
24	-18.97	0.9860	0.06244	0.1543	0.001076	0.05763
25	-18.96	0.9856	0.06469	0.1563	0.001311	0.05889
26	-18.93	0.9854	0.06447	0.1573	0.001550	0.05686
27	-18.98	0.9855	0.06487	0.1568	0.001828	0.05821
28	-18.97	0.9852	0.06480	0.1587	0.002056	0.05782
29	-18.94	0.9852	0.06438	0.1588	0.002052	0.05624
30	-18.89	0.9848	0.06371	0.1614	0.002102	0.05383
31	-18.84	0.9849	0.06574	0.1604	0.002289	0.05740
32	-18.91	0.9853	0.06504	0.1582	0.002322	0.05684
33	-18.94	0.9855	0.06414	0.1568	0.002349	0.05940
34	-18.96	0.9856	0.06216	0.1569	0.002225	0.05648
35	-18.95	0.9851	0.06419	0.1597	0.002649	0.06830
36	-18.95	0.9849	0.06237	0.1614	0.002799	0.05596
37	-18.89	0.9845	0.06350	0.1633	0.002843	0.05919
38	-18.87	0.9849	0.06108	0.1620	0.002706	0.05396
39	-18.84	0.9847	0.06264	0.1627	0.002848	0.05645
40	-18.94	0.9851	0.06052	0.1612	0.002817	0.05367
41	-18.92	0.9851	0.06204	0.1607	0.002910	0.05809
42	-18.90	0.9856	0.05983	0.1583	0.002756	0.05516
43	-18.96	0.9855	0.06083	0.1581	0.002885	0.05836
44	-18.94	0.9854	0.06041	0.1590	0.002891	0.05584
45	-18.95	0.9858	0.06025	0.1568	0.002908	0.06455
46	-18.90	0.9861	0.05771	0.1560	0.002773	0.05849
47	-18.91	0.9861	0.05807	0.1556	0.002822	0.06921
48	-18.91	0.9865	0.05494	0.1541	0.002727	0.05952
49	-18.95	0.9858	0.05695	0.1578	0.002868	0.05873
50	-18.92	0.9860	0.05616	0.1569	0.002755	0.05573
51	-18.93	0.9861	0.05624	0.1565	0.002733	0.06232
52	-18.91	0.9861	0.05514	0.1566	0.002694	0.05688
53	-18.89	0.9864	0.05450	0.1552	0.002717	0.05817
54	-18.87	0.9861	0.05481	0.1570	0.002853	0.05565
55	-18.90	0.9861	0.05484	0.1568	0.002843	0.05866
56	-18.93	0.9866	0.05316	0.1541	0.002646	0.05978
57	-18.92	0.9866	0.05261	0.1543	0.002559	0.05728
58	-18.92	0.9866	0.05189	0.1545	0.002451	0.05736
59	-18.92	0.9867	0.05059	0.1546	0.002325	0.06070
60	-18.60	0.9868	0.05234	0.1531	0.002831	0.06481
61	-18.90	0.9864	0.05136	0.1562	0.002656	0.06291
62	-18.97	0.9861	0.04991	0.1583	0.002647	0.05492
63	-18.94	0.9861	0.04994	0.1582	0.002713	0.06368
64	-18.97	0.9867	0.04787	0.1553	0.002674	0.05649
65	-18.97	0.9862	0.04959	0.1578	0.002785	0.06491
66	-18.96	0.9865	0.04724	0.1567	0.002695	0.05571
67	-18.98	0.9868	0.04627	0.1554	0.002636	0.05992
68	-18.95	0.9864	0.04527	0.1577	0.002587	0.05517

TABLE VIII. (Continued.)

$\Lambda = 4, \text{ibm_lagos}$						
Iteration	Energy	$ A_0 $	$ A_1 $	$ A_2 $	$ A_3 $	Bures distance
69	-18.97	0.9864	0.04607	0.1577	0.002678	0.05925
70	-18.96	0.9867	0.04401	0.1567	0.002654	0.05776
71	-18.93	0.9870	0.04284	0.1550	0.002585	0.05663
72	-18.93	0.9865	0.04322	0.1579	0.002611	0.05534
73	-18.91	0.9869	0.04026	0.1563	0.002455	0.05618
74	-18.94	0.9870	0.03932	0.1559	0.002338	0.05738
75	-18.97	0.9870	0.03816	0.1559	0.002348	0.05688
76	-18.88	0.9872	0.03828	0.1547	0.002434	0.05698
77	-18.91	0.9872	0.03856	0.1547	0.002462	0.05768
78	-18.93	0.9874	0.03741	0.1539	0.002335	0.05807
79	-18.93	0.9876	0.03743	0.1527	0.002344	0.06376
80	-18.92	0.9878	0.03655	0.1515	0.002298	0.06062

TABLE IX. Unprojected wave functions expressed in the full $\beta = 0$ basis, reconstructed from classical and quantum simulations in $\Lambda = 2, 4$ effective model spaces, along with the exact wave function. The LMG model parameters are $N = 30, \varepsilon = 1.0, \bar{v} = 2.0$. The projected ground-state wave functions can be obtained by setting the odd- n components to zero, and rescaling, as described in Sec. III.

Full-space wave functions (unprojected)					
State, n	Exact	AER $\Lambda = 2$	ibm_lagos $\Lambda = 2$	AER $\Lambda = 4$	ibm_lagos $\Lambda = 4$
1	0.064046	0.01337(15)	0.0139(16)	0.03390(62)	0.0321(33)
2	0.11405	0.04229(42)	0.0437(44)	0.0881(13)	0.0843(70)
3	0.17438	0.09298(78)	0.0957(82)	0.1594(19)	0.1541(99)
4	0.23289	0.1639(11)	0.167(11)	0.2330(20)	0.227(11)
5	0.28608	0.2459(13)	0.250(13)	0.2942(18)	0.290(10)
6	0.32693	0.3237(12)	0.327(12)	0.3348(12)	0.3344(76)
7	0.35138	0.38146(87)	0.3842(87)	0.35422(66)	0.3567(46)
8	0.35860	0.40774(31)	0.4085(28)	0.35635(27)	0.3605(18)
9	0.34752	0.39910(30)	0.3978(35)	0.34535(43)	0.3495(17)
10	0.32276	0.36020(82)	0.3572(87)	0.32343(84)	0.3261(46)
11	0.28598	0.3013(11)	0.297(11)	0.2914(12)	0.2922(75)
12	0.24395	0.2345(12)	0.230(12)	0.2508(15)	0.2498(98)
13	0.19892	0.1703(11)	0.166(11)	0.2045(17)	0.202(11)
14	0.15647	0.11572(97)	0.1125(98)	0.1570(17)	0.154(10)
15	0.11767	0.07361(73)	0.0712(73)	0.1130(15)	0.1107(97)
16	0.085371	0.04389(50)	0.0422(50)	0.0760(12)	0.0743(78)
17	0.059140	0.02453(31)	0.0235(31)	0.04778(93)	0.0465(57)
18	0.039465	0.01285(18)	0.0122(18)	0.02796(63)	0.0272(38)
19	0.025074	0.00630(10)	0.00599(99)	0.01522(38)	0.0148(23)
20	0.015295	0.002892(51)	0.00273(49)	0.00770(22)	0.0074(13)
21	0.0088408	0.001238(23)	0.00116(23)	0.00361(11)	0.00351(67)
22	0.0048782	0.000493(10)	0.000463(98)	0.001569(54)	0.00152(31)
23	0.0025309	0.0001821(40)	0.000170(38)	0.000627(23)	0.00061(13)
24	0.0012416	<0.0001	<0.0001	0.0002302(93)	0.000224(54)
25	0.00056553	<0.0001	<0.0001	<0.0001	<0.0001
26	0.00023956	<0.0001	<0.0001	<0.0001	<0.0001
27	<0.0001	<0.0001	<0.0001	<0.0001	<0.0001
28	<0.0001	<0.0001	<0.0001	<0.0001	<0.0001
29	<0.0001	<0.0001	<0.0001	<0.0001	<0.0001
30	<0.0001	<0.0001	<0.0001	<0.0001	<0.0001

TABLE X. The difference between the exact ground state energy and that obtained using HL-VQE with different truncations obtained with classical simulations (in units of ε). “Naive” indicates truncation of the Hamiltonian without modification, “Effective” indicates results from the effective model space, and “Effective projected” indicates results from the projected effective wave function. The LMG model parameters are $N = 32$, $\varepsilon = 1.0$, $\bar{v} = 2.0$.

$N = 32$			
Λ	Naive	Effective	Effective projected
2	4.1650	1.6497×10^{-1}	1.6497×10^{-1}
4	3.4144	1.5623×10^{-2}	1.5619×10^{-2}
6	2.4775	2.0314×10^{-3}	1.9222×10^{-3}
8	1.6218	6.9980×10^{-4}	2.3089×10^{-4}
10	9.5918×10^{-1}	5.5488×10^{-4}	2.4225×10^{-5}
12	4.9318×10^{-1}	5.3602×10^{-4}	4.0713×10^{-6}
14	2.0974×10^{-1}	5.3282×10^{-4}	9.5794×10^{-7}
16	6.9504×10^{-2}	5.3203×10^{-4}	2.3434×10^{-7}
18	1.7265×10^{-2}	5.3168×10^{-4}	1.2486×10^{-7}
20	3.6812×10^{-3}	5.3131×10^{-4}	3.5171×10^{-7}
22	8.9597×10^{-4}	5.2763×10^{-4}	1.0558×10^{-5}
24	7.4972×10^{-5}	7.4972×10^{-5}	7.4972×10^{-5}
26	3.7240×10^{-6}	3.7240×10^{-6}	3.7240×10^{-6}
28	9.6145×10^{-8}	9.6145×10^{-8}	9.6145×10^{-8}
30	9.7540×10^{-10}	9.7541×10^{-10}	9.7541×10^{-10}
32	0	0	0

TABLE XI. The difference between the exact ground state energy and that obtained using HL-VQE with different truncations obtained with classical simulations (in units of ε). “Naive” indicates truncation of the Hamiltonian without modification, “Effective” indicates results from the effective model space, and “Effective projected” indicates results from the projected effective wave function. The LMG model parameters are $N = 64$, $\varepsilon = 1.0$, $\bar{v} = 2.0$.

$N = 64$			
Λ	Naive	Effective	Effective projected
2	8.1569	1.5689×10^{-1}	1.5689×10^{-1}
4	7.4157	1.3157×10^{-2}	1.3157×10^{-2}
6	6.3471	1.0902×10^{-3}	1.0902×10^{-3}
8	5.2706	9.0117×10^{-5}	9.0117×10^{-5}
10	4.2615	7.7929×10^{-6}	7.7886×10^{-6}
12	3.3392	8.2237×10^{-7}	7.8705×10^{-7}
14	2.5243	2.0110×10^{-7}	9.6436×10^{-8}
16	1.8297	1.4181×10^{-7}	6.4595×10^{-9}
18	1.2606	1.3566×10^{-7}	9.1655×10^{-10}
20	8.1584×10^{-1}	1.3495×10^{-7}	1.0981×10^{-10}
22	4.8843×10^{-1}	1.3486×10^{-7}	1.6069×10^{-11}
24	2.6531×10^{-1}	1.3485×10^{-7}	2.9514×10^{-12}
26	1.2783×10^{-1}	1.3484×10^{-7}	6.7541×10^{-13}
28	5.3358×10^{-2}	1.3484×10^{-7}	1.8833×10^{-13}
30	1.8905×10^{-2}	1.3484×10^{-7}	6.1047×10^{-14}
32	5.6094×10^{-3}	1.3484×10^{-7}	2.5971×10^{-14}
34	1.3850×10^{-3}	1.3484×10^{-7}	8.9075×10^{-15}
36	2.8397×10^{-4}	1.3484×10^{-7}	9.2551×10^{-15}
38	4.8379×10^{-5}	1.3484×10^{-7}	7.0723×10^{-15}
40	6.9896×10^{-6}	1.3484×10^{-7}	4.9407×10^{-15}
42	1.0368×10^{-6}	1.3484×10^{-7}	4.7592×10^{-14}
44	2.3949×10^{-7}	1.3477×10^{-7}	2.7661×10^{-10}

TABLE XI. (Continued.)

$N = 64$			
Λ	Naive	Effective	Effective projected
46	1.9755×10^{-8}	1.9755×10^{-8}	1.9755×10^{-8}
48	1.2852×10^{-9}	1.2852×10^{-9}	1.2852×10^{-9}
50	6.445×10^{-11}	6.445×10^{-11}	6.445×10^{-11}
52	2.417×10^{-12}	2.417×10^{-12}	2.417×10^{-12}
54	6.5×10^{-14}	6.5×10^{-14}	6.5×10^{-14}
56	1.1×10^{-15}	1.1×10^{-15}	1.1×10^{-15}

TABLE XII. The difference between the exact ground state energy and that obtained using HL-VQE with different truncations obtained with classical simulations (in units of ε). “Naive” indicates truncation of the Hamiltonian without modification, “Effective” indicates results from the effective model space, and “Effective projected” indicates results from the projected effective wave function. A dash indicates a value below 10^{-15} , and all values for $74 < \Lambda < 96$ are below this value. The LMG model parameters are $N = 96$, $\varepsilon = 1.0$, $\bar{v} = 2.0$.

$N = 96$			
Λ	Naive	Effective	Effective projected
2	1.2155×10^1	1.5459×10^{-1}	1.5459×10^{-1}
4	1.1416×10^1	1.2629×10^{-2}	1.2629×10^{-2}
6	1.0304×10^1	9.9641×10^{-4}	9.9641×10^{-4}
8	9.1508	7.6372×10^{-5}	7.6372×10^{-5}
10	8.0154	5.8604×10^{-6}	5.8604×10^{-6}
12	6.9164	4.5826×10^{-7}	4.5826×10^{-7}
14	5.8757	3.6940×10^{-8}	3.6940×10^{-8}
16	4.9088	3.1168×10^{-9}	3.1151×10^{-9}
18	4.0261	2.9945×10^{-10}	2.9098×10^{-10}
20	3.2338	5.4361×10^{-11}	3.3224×10^{-11}
22	2.5358	3.2170×10^{-11}	3.6422×10^{-12}
24	1.9334	2.9776×10^{-11}	2.1585×10^{-13}
26	1.4260	2.9563×10^{-11}	3.9432×10^{-14}
28	1.0109	2.9534×10^{-11}	9.3732×10^{-15}
30	6.8338×10^{-1}	2.9527×10^{-11}	2.5873×10^{-15}
32	4.3622×10^{-1}	2.9541×10^{-11}	—
34	2.5994×10^{-1}	2.9527×10^{-11}	—
36	1.4276×10^{-1}	2.9527×10^{-11}	—
38	7.1321×10^{-2}	2.9520×10^{-11}	—
40	3.2037×10^{-2}	2.9520×10^{-11}	—
42	1.2829×10^{-2}	2.9520×10^{-11}	—
44	4.5583×10^{-3}	2.9520×10^{-11}	—
46	1.4350×10^{-3}	2.9534×10^{-11}	—
48	4.0038×10^{-4}	2.9520×10^{-11}	—
50	9.9070×10^{-5}	2.9527×10^{-11}	—
52	2.1741×10^{-5}	2.9527×10^{-11}	—
54	4.2285×10^{-6}	2.9527×10^{-11}	—
56	7.2773×10^{-7}	2.9520×10^{-11}	—
58	1.1060×10^{-7}	2.9520×10^{-11}	—
60	1.4833×10^{-8}	2.9534×10^{-11}	—
62	1.7895×10^{-9}	2.9520×10^{-11}	—
64	2.3580×10^{-10}	2.9527×10^{-11}	—
66	5.3561×10^{-11}	2.9527×10^{-11}	—
68	4.4042×10^{-12}	4.4096×10^{-12}	4.4096×10^{-12}
70	3.1050×10^{-13}	5.0871×10^{-13}	5.0871×10^{-13}
72	1.8596×10^{-14}	1.8431×10^{-14}	1.8431×10^{-14}

- [1] R. Landauer, Irreversibility and heat generation in the computing process, *IBM J. Res. Dev.* **5**, 183 (1961).
- [2] C. H. Bennett, Logical reversibility of computation, *IBM J. Res. Dev.* **17**, 525 (1973).
- [3] P. Benioff, The computer as a physical system: A microscopic quantum mechanical Hamiltonian model of computers as represented by Turing machines, *J. Stat. Phys.* **22**, 563 (1980).
- [4] Y. Manin, *Computable and Uncomputable* (Sovetskoye Radio, Moscow, 1980).
- [5] R. P. Feynman, Simulating physics with computers, *Int. J. Theor. Phys.* **21**, 467 (1982).
- [6] E. Fredkin and T. Toffoli, Conservative logic, *Int. J. Theor. Phys.* **21**, 219 (1982).
- [7] R. P. Feynman, Quantum mechanical computers, *Found. Phys.* **16**, 507 (1986).
- [8] R. Landauer, Information is physical, *Phys. Today* **44**(5), 23 (1991).
- [9] C. P. Williams, *Quantum Computing and Quantum Communications*, First NASA International Conference, QCQC '98, Palm Springs, February 17–20, 1988, Selected Papers (Springer, Berlin, 1998).
- [10] S. Lloyd, Universal quantum simulators, *Science* **273**, 1073 (1996).
- [11] J. Kempe, A. Kitaev, and O. Regev, The complexity of the local hamiltonian problem, in *FSTTCS 2004: Foundations of Software Technology and Theoretical Computer Science*, edited by K. Lodaya and M. Mahajan (Springer, Berlin, 2005), pp. 372–383.
- [12] J. Preskill, Quantum Computing in the NISQ era and beyond, *Quantum* **2**, 79 (2018).
- [13] N. Klco, A. Roggero, and M. J. Savage, Standard model physics and the digital quantum revolution: Thoughts about the interface, *Rep. Prog. Phys.* **85**, 064301 (2022).
- [14] S. R. Beane, K. Orginos, and M. J. Savage, Hadronic interactions from lattice QCD, *Int. J. Mod. Phys. E* **17**, 1157 (2008).
- [15] S. R. Beane, W. Detmold, K. Orginos, and M. J. Savage, Nuclear physics from lattice QCD, *Prog. Part. Nucl. Phys.* **66**, 1 (2011).
- [16] Z. Davoudi, W. Detmold, K. Orginos, A. Parreño, M. J. Savage, P. Shanahan, and M. L. Wagman, Nuclear matrix elements from lattice QCD for electroweak and beyond-Standard-Model processes, *Phys. Rep.* **900**, 1 (2021).
- [17] C. Drischler, W. Haxton, K. McElvain, E. Mereghetti, A. Nicholson, P. Vranas, and A. Walker-Loud, Towards ground-state nuclear physics in QCD, *Prog. Part. Nucl. Phys.* **121**, 103888 (2021).
- [18] S. Weinberg, Phenomenological Lagrangians, *Physica A* **96**, 327 (1979).
- [19] J. Gasser and H. Leutwyler, Chiral perturbation theory to one loop, *Ann. Phys. (NY)* **158**, 142 (1984).
- [20] E. E. Jenkins and A. V. Manohar, Baryon chiral perturbation theory using a heavy fermion Lagrangian, *Phys. Lett. B* **255**, 558 (1991).
- [21] S. Weinberg, Nuclear forces from chiral Lagrangians, *Phys. Lett. B* **251**, 288 (1990).
- [22] U. van Kolck, Few nucleon forces from chiral Lagrangians, *Phys. Rev. C* **49**, 2932 (1994).
- [23] D. B. Kaplan, M. J. Savage, and M. B. Wise, A New expansion for nucleon-nucleon interactions, *Phys. Lett. B* **424**, 390 (1998).
- [24] E. Epelbaum, W. Gloeckle, and U.-G. Meissner, Nuclear forces from chiral Lagrangians using the method of unitary transformation. 1. Formalism, *Nucl. Phys. A* **637**, 107 (1998).
- [25] H. Hergert, A guided tour of ab initio nuclear many-body theory, *Front. Phys.* **8**, 379 (2020).
- [26] M. J. Savage, Nuclear physics from QCD: The anticipated impact of exa-scale computing, in *The IX International Conference on Quark Confinement and the Hadron Spectrum—QCXS IX*, 30 August–3 September 2010, Madrid, AIP Conf. Proc. No. 1343 (AIP, New York, 2011), pp. 30–38.
- [27] B. Şahinoğlu and R. D. Somma, Hamiltonian simulation in the low-energy subspace, *npj Quantum Inf.* **7**, 119 (2021).
- [28] T. Papenbrock and D. J. Dean, Factorization of shell-model ground states, *Phys. Rev. C* **67**, 051303(R) (2003).
- [29] T. Papenbrock, A. Juodagalvis, and D. J. Dean, Solution of large scale nuclear structure problems by wave function factorization, *Phys. Rev. C* **69**, 024312 (2004).
- [30] T. Papenbrock and D. J. Dean, Density matrix renormalization group and wavefunction factorization for nuclei, *J. Phys. G: Nucl. Part. Phys.* **31**, S1377 (2005).
- [31] Ö. Legeza, L. Veis, A. Poves, and J. Dukelsky, Advanced density matrix renormalization group method for nuclear structure calculations, *Phys. Rev. C* **92**, 051303(R) (2015).
- [32] C. W. Johnson and O. C. Gorton, Proton-neutron entanglement in the nuclear shell model, *J. Phys. G* **50**, 045110 (2023).
- [33] C. Robin, M. J. Savage, and N. Pillet, Entanglement rearrangement in self-consistent nuclear structure calculations, *Phys. Rev. C* **103**, 034325 (2021).
- [34] A. T. Kruppa, J. Kovács, P. Salamon, and O. Legeza, Entanglement and correlation in two-nucleon systems, *J. Phys. G: Nucl. Part. Phys.* **48**, 025107 (2021).
- [35] A. T. Kruppa, J. Kovács, P. Salamon, O. Legeza, and G. Zaránd, Entanglement and seniority, *Phys. Rev. C* **106**, 024303 (2022).
- [36] J. Faba, V. Martín, and L. Robledo, Two-orbital quantum discord in fermion systems, *Phys. Rev. A* **103**, 032426 (2021).
- [37] J. Faba, V. Martín, and L. Robledo, Correlation energy and quantum correlations in a solvable model, *Phys. Rev. A* **104**, 032428 (2021).
- [38] J. Faba, V. Martín, and L. Robledo, Analysis of quantum correlations within the ground state of a three-level Lipkin model, *Phys. Rev. A* **105**, 062449 (2022).
- [39] E. Pazy, Entanglement entropy between short range correlations and the Fermi sea in nuclear structure, *Phys. Rev. C* **107**, 054308 (2023).
- [40] A. Tichai, S. Knecht, A. T. Kruppa, O. Legeza, C. P. Moca, A. Schwenk, M. A. Werner, and G. Zarand, Combining the in-medium similarity renormalization group with the density matrix renormalization group: Shell structure and information entropy, [arXiv:2207.01438](https://arxiv.org/abs/2207.01438).
- [41] A. Bulgac, M. Kafker, and I. Abdurrahman, Measures of complexity and entanglement in many-fermion systems, *Phys. Rev. C* **107**, 044318 (2023).
- [42] A. Bulgac, Entanglement entropy, single-particle occupation probabilities, and short-range correlations, *Phys. Rev. C* **107**, L061602 (2023).
- [43] J. Vidal, G. Palacios, and R. Mosseri, Entanglement in a second-order quantum phase transition, *Phys. Rev. A* **69**, 022107 (2004).

- [44] J. Vidal, R. Mosseri, and J. Dukelsky, Entanglement in a first-order quantum phase transition, *Phys. Rev. A* **69**, 054101 (2004).
- [45] J. Vidal, G. Palacios, and C. Aslangul, Entanglement dynamics in the Lipkin-Meshkov-Glick model, *Phys. Rev. A* **70**, 062304 (2004).
- [46] J. I. Latorre, R. Orús, E. Rico, and J. Vidal, Entanglement entropy in the Lipkin-Meshkov-Glick model, *Phys. Rev. A* **71**, 064101 (2005).
- [47] H. T. Cui, Multiparticle entanglement in the Lipkin-Meshkov-Glick model, *Phys. Rev. A* **77**, 052105 (2008).
- [48] M. Di Tullio, R. Rossignoli, M. Cerezo, and N. Gigena, Fermionic entanglement in the Lipkin model, *Phys. Rev. A* **100**, 062104 (2019).
- [49] M. J. Cervia, A. B. Balantekin, S. N. Coppersmith, C. W. Johnson, P. J. Love, C. Poole, K. Robbins, and M. Saffman, Lipkin model on a quantum computer, *Phys. Rev. C* **104**, 024305 (2021).
- [50] A. Chikaoka and H. Liang, Quantum computing for the Lipkin model with unitary coupled cluster and structure learning ansatz, *Chin. Phys. C* **46**, 024106 (2022).
- [51] A. M. Romero, J. Engel, H. L. Tang, and S. E. Economou, Solving nuclear structure problems with the adaptive variational quantum algorithm, *Phys. Rev. C* **105**, 064317 (2022).
- [52] M. Q. Hlatshwayo, Y. Zhang, H. Wibowo, R. LaRose, D. Lacroix, and E. Litvinova, Simulating excited states of the Lipkin model on a quantum computer, *Phys. Rev. C* **106**, 024319 (2022).
- [53] IBM Quantum, <https://quantum-computing.ibm.com/>, 2021.
- [54] H. R. Grimsley, S. E. Economou, E. Barnes, and N. J. Mayhall, An adaptive variational algorithm for exact molecular simulations on a quantum computer, *Nat. Commun.* **10**, 3007 (2019).
- [55] P. G. Anastasiou, Y. Chen, N. J. Mayhall, E. Barnes, and S. E. Economou, TETRIS-ADAPT-VQE: An adaptive algorithm that yields shallower, denser circuit ansätze, [arXiv:2209.10562](https://arxiv.org/abs/2209.10562).
- [56] I. O. Sokolov, P. K. Barkoutsos, P. J. Ollitrault, D. Greenberg, J. Rice, M. Pistoia, and I. Tavernelli, Quantum orbital-optimized unitary coupled cluster methods in the strongly correlated regime: Can quantum algorithms outperform their classical equivalents?, *J. Chem. Phys.* **152**, 124107 (2020).
- [57] W. Mizukami, K. Mitarai, Y. O. Nakagawa, T. Yamamoto, T. Yan, and Y.-y. Ohnishi, Orbital optimized unitary coupled cluster theory for quantum computer, *Phys. Rev. Res.* **2**, 033421 (2020).
- [58] M. Treinish, J. Gambetta, P. Nation, qiskit bot, P. Kassebaum, D. M. Rodríguez, S. de la Puente González, S. Hu, K. Krsulich, J. Lishman, J. Garrison, L. Zdanski, J. Yu, M. Marques, J. Gacon, D. McKay, J. Gomez, L. Capelluto, Travis-S-IBM, A. Panigrahi, lerongil, R. I. Rahman, S. Wood, L. Bello, T. Itoko, C. J. Wood, D. Singh, Drew, E. Arbel, and Glen, Qiskit/qiskit: Qiskit 0.37.1, Zenodo (2022), doi: [10.5281/zenodo.6924865](https://doi.org/10.5281/zenodo.6924865).
- [59] H. Lipkin, N. Meshkov, and A. Glick, Validity of many-body approximation methods for a solvable model: (I). Exact solutions and perturbation theory, *Nucl. Phys.* **62**, 188 (1965).
- [60] E. Knill, R. Laflamme, and G. Milburn, Efficient linear optics quantum computation, [arXiv:quant-ph/0006088](https://arxiv.org/abs/quant-ph/0006088); A scheme for efficient quantum computation with linear optics, *Nature* **409**, 46 (2001).
- [61] T. C. Ralph, A. J. F. Hayes, and A. Gilchrist, Loss-Tolerant Optical Qubits, *Phys. Rev. Lett.* **95**, 100501 (2005).
- [62] P. G. Szalay, T. Müller, G. Gidofalvi, H. Lischka, and R. Shepard, Multiconfiguration self-consistent field and multireference configuration interaction methods and applications, *Chem. Rev.* **112**, 108 (2012).
- [63] C. Robin, N. Pillet, D. Peña Arteaga, and J. F. Berger, Description of nuclear systems with a self-consistent configuration-mixing approach: Theory, algorithm, and application to the ^{12}C test nucleus, *Phys. Rev. C* **93**, 024302 (2016).
- [64] C. Robin, N. Pillet, M. Dupuis, J. Le Bloas, D. Peña Arteaga, and J. F. Berger, Description of nuclear systems with a self-consistent configuration-mixing approach. II: Application to structure and reactions in even-even *sd*-shell nuclei, *Phys. Rev. C* **95**, 044315 (2017).
- [65] A. Edmonds, *Angular Momentum in Quantum Mechanics*, Investigations in Physics (Princeton University Press, Princeton, 2016).
- [66] P. Ring and P. Schuck, *The Nuclear Many-Body Problem* (Springer, Berlin, 2004).
- [67] D. Lacroix, Symmetry-Assisted Preparation of Entangled Many-Body States on a Quantum Computer, *Phys. Rev. Lett.* **125**, 230502 (2020).
- [68] E. A. Ruiz Guzman and D. Lacroix, Accessing ground-state and excited-state energies in a many-body system after symmetry restoration using quantum computers, *Phys. Rev. C* **105**, 024324 (2022).
- [69] D. Lacroix, E. A. Ruiz Guzman, and P. Siwach, Symmetry breaking/symmetry preserving circuits and symmetry restoration on quantum computers: A quantum many-body perspective, *Eur. Phys. J. A* **59**, 3 (2023).
- [70] E. A. R. Guzman and D. Lacroix, Restoring broken symmetries using quantum search “oracles”, *Phys. Rev. C* **107**, 034310 (2023).
- [71] D. Bures, An extension of Kakutani’s theorem on infinite product measures to the tensor product of semifinite w^* -algebras, *Trans. Am. Math. Soc.* **135**, 199 (1969).
- [72] D. Agassi, H. Lipkin, and N. Meshkov, Validity of many-body approximation methods for a solvable model: (IV). The deformed Hartree-Fock solution, *Nucl. Phys.* **86**, 321 (1966).
- [73] D. P. Kingma and J. Ba, Adam: A method for stochastic optimization, [arXiv:1412.6980](https://arxiv.org/abs/1412.6980).
- [74] J. Duchi, E. Hazan, and Y. Singer, Adaptive subgradient methods for online learning and stochastic optimization, *J. Mach. Learn. Res.* **12**, 2121 (2011).
- [75] H.-Y. Huang, R. Kueng, and J. Preskill, Predicting many properties of a quantum system from very few measurements, *Nat. Phys.* **16**, 1050 (2020).
- [76] H.-Y. Huang, R. Kueng, G. Torlai, V. V. Albert, and J. Preskill, Provably efficient machine learning for quantum many-body problems, *Science* **377**, 682 (2022).
- [77] N. Klco and M. J. Savage, Minimally entangled state preparation of localized wave functions on quantum computers, *Phys. Rev. A* **102**, 012612 (2020).
- [78] P. Besserve and T. Ayrál, Unraveling correlated material properties with noisy quantum computers: Natural orbitalized variational quantum eigensolving of extended impurity models within a slave-boson approach, *Phys. Rev. B* **105**, 115108 (2022).
- [79] S. P. Jordan, K. S. M. Lee, and J. Preskill, Quantum algorithms for quantum field theories, *Science* **336**, 1130 (2012).

- [80] S. P. Jordan, K. S. M. Lee, and J. Preskill, Quantum computation of scattering in scalar quantum field theories, *Quantum Inf. Comput.* **14**, 1014 (2014).
- [81] S. P. Jordan, H. Krovi, K. S. M. Lee, and J. Preskill, BQP-completeness of scattering in scalar quantum field theory, *Quantum* **2**, 44 (2018).
- [82] N. Klco and M. J. Savage, Digitization of scalar fields for quantum computing, *Phys. Rev. A* **99**, 052335 (2019).
- [83] Y. Li and S. C. Benjamin, Efficient Variational Quantum Simulator Incorporating Active Error Minimization, *Phys. Rev. X* **7**, 021050 (2017).
- [84] N. Klco, E. F. Dumitrescu, A. J. McCaskey, T. D. Morris, R. C. Pooser, M. Sanz, E. Solano, P. Lougovski, and M. J. Savage, Quantum-classical computation of Schwinger model dynamics using quantum computers, *Phys. Rev. A* **98**, 032331 (2018).
- [85] J. J. Wallman and J. Emerson, Noise tailoring for scalable quantum computation via randomized compiling, *Phys. Rev. A* **94**, 052325 (2016).
- [86] L. Viola and S. Lloyd, Dynamical suppression of decoherence in two-state quantum systems, *Phys. Rev. A* **58**, 2733 (1998).
- [87] L.-M. Duan and G.-C. Guo, Suppressing environmental noise in quantum computation through pulse control, *Phys. Lett. A* **261**, 139 (1999).
- [88] P. Zanardi, Symmetrizing evolutions, *Phys. Lett. A* **258**, 77 (1999).
- [89] L. Viola, E. Knill, and S. Lloyd, Dynamical Decoupling of Open Quantum Systems, *Phys. Rev. Lett.* **82**, 2417 (1999).
- [90] M. Urbanek, B. Nachman, V. R. Pascuzzi, A. He, C. W. Bauer, and W. A. de Jong, Mitigating Depolarizing Noise on Quantum Computers with Noise-Estimation Circuits, *Phys. Rev. Lett.* **127**, 270502 (2021).
- [91] S. A. Rahman, R. Lewis, E. Mendicelli, and S. Powell, Self-mitigating Trotter circuits for SU(2) lattice gauge theory on a quantum computer, *Phys. Rev. D* **106**, 074502 (2022).
- [92] R. C. Farrell, I. A. Chernyshev, S. J. M. Powell, N. A. Zemlevskiy, M. Illa, and M. J. Savage, Preparations for quantum simulations of quantum chromodynamics in 1+1 dimensions. I. Axial gauge, *Phys. Rev. D* **107**, 054512 (2023).
- [93] K. Yeter-Aydeniz, Z. Parks, A. Nair, E. Gustafson, A. F. Kemper, R. C. Pooser, Y. Meurice, and P. Dreher, Measuring NISQ gate-based qubit stability using a 1+1 field theory and cycle benchmarking, [arXiv:2201.02899](https://arxiv.org/abs/2201.02899).
- [94] M. C. Bañuls *et al.*, Simulating lattice gauge theories within quantum technologies, *Eur. Phys. J. D* **74**, 165 (2020).
- [95] J. Kogut and L. Susskind, Hamiltonian formulation of Wilson's lattice gauge theories, *Phys. Rev. D* **11**, 395 (1975).
- [96] G. Pardo, T. Greenberg, A. Fortinsky, N. Katz, and E. Zohar, Resource-efficient quantum simulation of lattice gauge theories in arbitrary dimensions: Solving for Gauss's law and fermion elimination, *Phys. Rev. Res.* **5**, 023077 (2023).
- [97] R. Kaubruegger, D. V. Vasilyev, M. Schulte, K. Hammerer, and P. Zoller, Quantum Variational Optimization of Ramsey Interferometry and Atomic Clocks, *Phys. Rev. X* **11**, 041045 (2021).
- [98] D-Wave Systems Inc., D-Wave System Documentation, <https://docs.dwavesys.com/docs/latest/index.html>.
- [99] <https://itconnect.uw.edu/research/hpc>.
- [100] <https://phys.washington.edu>.
- [101] <https://www.artsci.washington.edu>.
- [102] G. Van Rossum and F. L. Drake, *Python 3 Reference Manual* (CreateSpace, Scotts Valley, CA, 2009).
- [103] F. Pérez and B. E. Granger, IPython: A system for interactive scientific computing, *Comput. Sci. Eng.* **9**, 21 (2007).
- [104] Wolfram Research, Inc., Champaign, IL, *Mathematica*, Version 12.3.10, 2022.
- [105] M. Illa and M. J. Savage, Basic elements for simulations of standard-model physics with quantum annealers: Multigrid and clock states, *Phys. Rev. A* **106**, 052605 (2022).
- [106] R. Colle and O. Salvetti, Multiconfiguration-self-consistent field (MC-SCF) method for excited states, *Mol. Phys.* **47**, 959 (1982).
- [107] J. Hinze and F. F. Chemie, Developments in the calculation of electronic wavefunctions for molecules: MCSCF, CI, and numerical SCF for molecules, *Int. J. Quantum Chem.* **20**, 69 (1981).
- [108] M. P. Deskevich, D. J. Nesbitt, and H.-J. Werner, Dynamically weighted multiconfiguration self-consistent field: Multistate calculations for $F + H_2O \rightarrow HF + OH$ reaction paths, *J. Chem. Phys.* **120**, 7281 (2004).